Nanoscale

REVIEW

View Article Online
View Journal | View Issue

Cite this: *Nanoscale*, 2022, **14**, 15560

Alloying strategies for tuning product selectivity during electrochemical CO_2 reduction over Cu

Venkata Sai Sriram Mosali,[a] Alan M. Bond [a,b] and Jie Zhang *[a,b]

Received 28th June 2022,
Accepted 5th October 2022

DOI: 10.1039/d2nr03539a

rsc.li/nanoscale

Excessive reliance on fossil fuels has led to the release and accumulation of large quantities of CO_2 into the atmosphere which has raised serious concerns related to environmental pollution and global warming. One way to mitigate this problem is to electrochemically recycle CO_2 to value-added chemicals or fuels using electricity from renewable energy sources. Cu is the only metallic electrocatalyst that has been shown to produce a wide range of industrially important chemicals at appreciable rates. However, low product selectivity is a fundamental issue limiting commercial applications of electrochemical CO_2 reduction over Cu catalysts. Combining copper with other metals that actively contribute to the electrochemical CO_2 reduction reaction process can selectively facilitate generation of desirable products. Alloying Cu can alter surface binding strength through electronic and geometric effects, enhancing the availability of surface confined carbon species, and stabilising key reduction intermediates. As a result, significant research has been undertaken to design and fabricate copper-based alloy catalysts with structures that can enhance the selectivity of targeted products. In this article, progress with use of alloying strategies for development of Cu-alloy catalysts are reviewed. Challenges in achieving high selectivity and possible future directions for development of new copper-based alloy catalysts are considered.

1. Introduction

Carbon dioxide (CO_2) is a greenhouse gas that is a major contributor to global warming. In recent years, the concentration of CO_2 in the atmosphere has increased rapidly, resulting in the rise of global temperatures, which disturbs the ecological balance. In nature, the CO_2 released into the atmosphere by natural processes is utilised by terrestrial plants and aquatic species, thus achieving a carbon balance. However, excessive dependency on fossil fuels in the modern chemical industry, particularly the automobile and electricity generation sectors, has led to the accumulation of additional CO_2 in the atmosphere.[1] In a recent report, the National Oceanic and Atmospheric Administration (NOAA) global monitoring laboratory advised of a 2.3 ppm surge in CO_2 levels in 2020 to 2021 period leading to an average level of 419 ppm in 2021.[2] Fig. 1 shows the global monthly mean CO_2 emissions in the atmosphere from 1980 until May 2022 reported by NOAA which reveal the seriousness of the carbon accumulation problem. However, if an effective CO_2 capture, storage and conversion to chemical fuels technologies can be developed, the CO_2 can be recycled. Ideally, if CO_2 is sourced directly through air or bioenergy carbon capture and storage and reacted with renewable H_2, the carbon cycle can be closed.[3]

A range of methods such as photochemical,[4–7] biochemical,[8–10] and photo-/thermochemical,[11–15] have been explored for conversion of CO_2 to value added chemicals or fuels. However, their success is highly sensitive to the reaction environment.[16] Another possibility is use of the electrochemical CO_2 reduction reaction (eCO_2RR) which can be per-

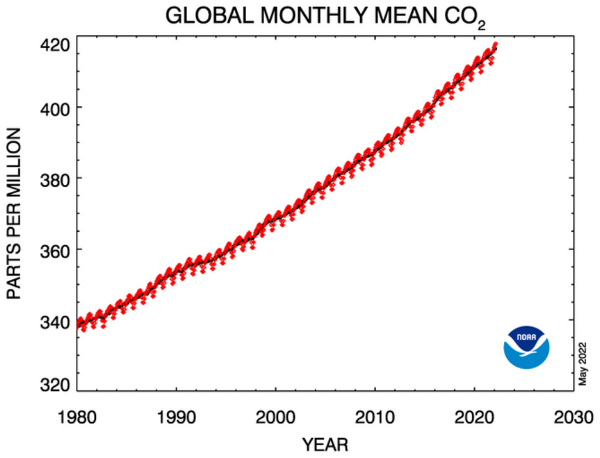

Fig. 1 Monthly mean CO_2 emissions from 1980 to May 2022 as reported by the NOAA global monitoring laboratory.[2]

---

[a] *School of Chemistry, Monash University, Clayton 3800, Victoria, Australia. E-mail: jie.zhang@monash.edu*

[b] *ARC Centre of Excellence for Electromaterials Science, Monash University, Clayton 3800, Victoria, Australia*

formed under ambient conditions using non-toxic materials and electrical energy from renewable sources, making it a highly desirable approach.[17]

The eCO_2RR can be performed in aqueous and non-aqueous media where the former are attractive in terms of non-toxicity, low cost, good conductivity, high proton availability and eco-friendliness. Aqueous electrolytes used are generally alkali salts comprising Na^+, K^+, Li^+, Rb^+, or Cs^+ cations and OH^-, HCO_3^-, Cl^-, $H_2PO_4^-$ or SO_4^{2-} anions. Both cations and anions can have a strong impact on the efficiency of eCO_2RR as well as product selectivity.[18–21] Additionally, other factors, such as temperature and pH (more critically local pH, since it can differ substantially from the bulk value, especially under high current density/low buffer capacity conditions) also influence the product selectivity during the eCO_2RR.[22–24] Table 1 provides several examples of eCO_2RR products generated in aqueous media and their reversible potentials ($E^{\circ\prime}$) *vs.* the reversible hydrogen electrode (RHE). Significant drawbacks of eCO_2RR in aqueous solutions are the low solubility of CO_2 resulting in low current densities, the presence of a competitive hydrogen evolution reaction (HER) which suppresses the overall eCO_2RR efficiency, in addition to sluggish kinetics and hence a large overpotential required to produce commercially desirable products at a sufficient rate.[17,21,25]

To date, three types of electrolysers have been mainly used for the eCO_2RR. The H-cell is most commonly used since it is easy to construct and facilitates rapid screening of catalysts and electrolyte composition. Fig. 2(a) shows a conventional H-cell for eCO_2RR. In this, the aqueous electrolytes used in most cases in both anodic and cathodic compartments are pre-saturated with CO_2. The cell is then sealed prior to performing electrolysis allowing gaseous products to be collected and quantified. The solubility of molecular CO_2 in these electrolytes is around 30 mM at 1 bar and thus the rate of CO_2 reduction is limited with a current density of typically less than 100 mA cm^{-2}.[26] To overcome the drawback of the low mass transport rate associated with the H-cell, electrolysers equipped with a gas diffusion electrode (GDE) have been developed. In these electrolysers, the CO_2 gas is diffused through a thin electrolyte layer on the GDE, with the diffusion length being ~50 nm.[27] The much higher mass transport rate achieved under these conditions allows an industrially appropriate current density of above 0.5 A cm^{-2} to be achieved.[27–29] Two types of such electrolysers are commonly used; the flow-cell and membrane electrode assembly (also known as zero-gap) electrolysers. To fabricate a GDE, a gas diffusion layer (GDL) is coated with a layer of catalyst. GDLs composed of carbon fibers possess high porosity.[30,31] The structure of the GDE has an impact on the transport of both reactants and products, which affects chemical species adsorption and depletion at the catalyst surface, and hence the overall eCO_2RR performance.[31,32]

Table 1 Electrochemical reactions relevant to eCO_2RR and their reversible potentials.[17]

Half-cell reaction	$E^{\circ\prime}$ (V *vs.* RHE)
$CO_2 + 2H^+ + 2e^- \rightarrow HCOOH(aq)$	−0.12
$CO_2 + 2H^+ + 2e^- \rightarrow CO(g) + H_2O$	−0.10
$CO_2 + 6H^+ + 6e^- \rightarrow CH_3OH(aq) + H_2O$	0.03
$CO_2 + 8H^+ + 8e^- \rightarrow CH_4(g) + 2H_2O$	0.17
$2CO_2 + 8H^+ + 8e^- \rightarrow CH_3COOH(aq) + 2H_2O$	0.11
$2CO_2 + 10H^+ + 10e^- \rightarrow CH_3CHO\ (aq) + 3H_2O$	0.06
$2CO_2 + 12H^+ + 12e^- \rightarrow C_2H_4(g) + 4H_2O$	0.08
$2CO_2 + 12H^+ + 12e^- \rightarrow C_2H_5OH(aq) + 3H_2O$	0.09
$2CO_2 + 14H^+ + 14e^- \rightarrow C_2H_6(g) + 4H_2O$	0.14
$3CO_2 + 16H^+ + 16e^- \rightarrow C_2H_5CHO(aq) + 5H_2O$	0.09
$3CO_2 + 18H^+ + 18e^- \rightarrow C3H_7OH(aq) + 5H_2O$	0.10

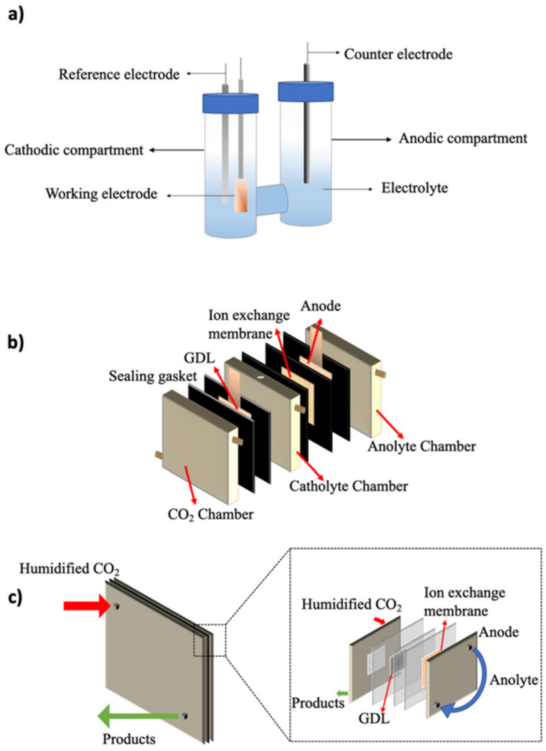

Fig. 2 Illustration of (a) H-cell, (b) flow cell and (c) zero gap MEA electrolysers used for eCO_2RR.

Properties such as porosity, electrical conductivity and hydrophobicity of the GDLs are now being tailored to improve the cell performance.[30] A typical flow-cell electrolyser is shown in Fig. 2(b) and consists of three channels, one for the CO_2 gas flow and the other two for electrolyte (catholyte and anolyte). The GDE is placed in between the CO_2 gas and catholyte channels. The catholyte and anolyte are separated by a polymer exchange membrane (PEM). The PEM used in the cell also greatly impacts the efficiency of the electrolyser. Cation exchange membranes (CEM) and anion exchange membranes (AEM) are the two types of PEM used depending on the reaction environment. Nafion, a CEM, was explored for eCO_2RR by Delacourt *et al.*[33] and found to suffer from excessive H_2 production and lack of stability in long-term electrolysis. AEMs are better suited for eCO_2RR circumstances because neutral or alkaline media can be used to minimize the competing H_2 evolution reaction. Since anions are far less mobile than protons, both in solution and in the membrane, an additional driving force (*i.e.* larger overpotential) is needed to overcome the resistance effect. Further, the transport of bicarbonate ions away from the cathode also diminishes the eCO_2RR performance.[30,34,35] The ratio of CO_2 and the proton source in a flow cell electrolyser is significantly higher than that found in an H-cell electrolyser. Furthermore, during the eCO_2RR, CO_2 is reduced and protons are consumed. Hence, the local reaction environment under the flow-cell conditions may be drastically different from that found under H-cell conditions due to its inherently higher CO_2 mass transport rate and hence higher current density. Accordingly, the results obtained with an H-cell may not be applicable under flow-cell conditions. Consequently, eCO_2RR performance ideally should be assessed under commercially relevant conditions using a flow cell-electrolyser. H-cell and flow-cell electrolysers are mainly used for fundamental research. The presence of a reference electrode in these configurations allows the anode and cathode to be investigated separately. In commercial applications, a reference electrode is not needed. A membrane electrode assembly (MEA) electrolyser is commonly used, inspired by developments of fuel cells, a closely related research area. A MEA electrolyser is composed of two channels, one for CO_2 and the other for anolyte (Fig. 2c). The PEM is sandwiched between the anode and the cathode to minimize the cell resistance. Use of a MEA electrolyser allows the full cell performance, including energy efficiency, to be evaluated.

The catalyst employed in an eCO_2RR is critical in determining the eCO_2RR product selectivity.[36] During electrolysis, the CO_2 molecule commonly is adsorbed onto the catalyst present in the cathode. Accordingly, the CO_2 reduction pathway usually depends on the binding strength of CO_2 and its reduced intermediates over the catalyst surface, as depicted in Fig. 3 and 4. CO_2 adsorbed on the catalyst is initially reduced to either carbonyl (*COOH) (an asterisk is used to indicate an adsorbed species) or formyl (*OCHO) intermediates in aqueous electrolyte which can be further reduced to CO and formate, respectively. CO is electroactive. However, if CO binds to the catalyst too strongly, then further reduction to desirable products and their subsequent desorption is inhibited. Poisoning of the catalyst also is likely to occur. Consequently, hydrogen evolution rather than CO_2 reduction may become the favoured reduction pathway. This scenario occurs at Pt, Ni, and Fe electrodes.[37] Alternatively, if the *CO binding ability to the catalyst is weak, as applies with metals such as Zn, Au, and Ag, then high selectivity for CO as the product is achieved.[37] If the catalyst has moderate binding strength for *CO, further reduction is facilitated, leading to more reduced carbon products. Cu is the only catalyst that has moderate *CO binding energy, leading to unique prospects for formation of a wide range of products. Metals which bind eCO_2RR intermediates too weakly are also likely to bind *H weakly. If these catalysts also possess strong *O affinity, an O-bound *OCHO intermediate will be formed during the initial reaction step which leads to formation of HCOOH.

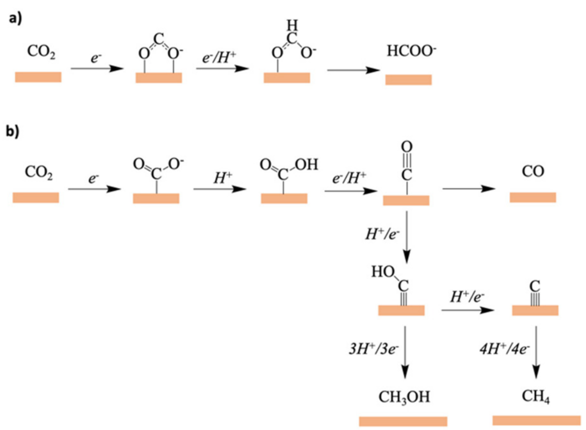

Fig. 3 Illustration of eCO_2RR pathways for the formation of (a) $HCOO^-$, (b) CO, CH_3OH, CH_4.

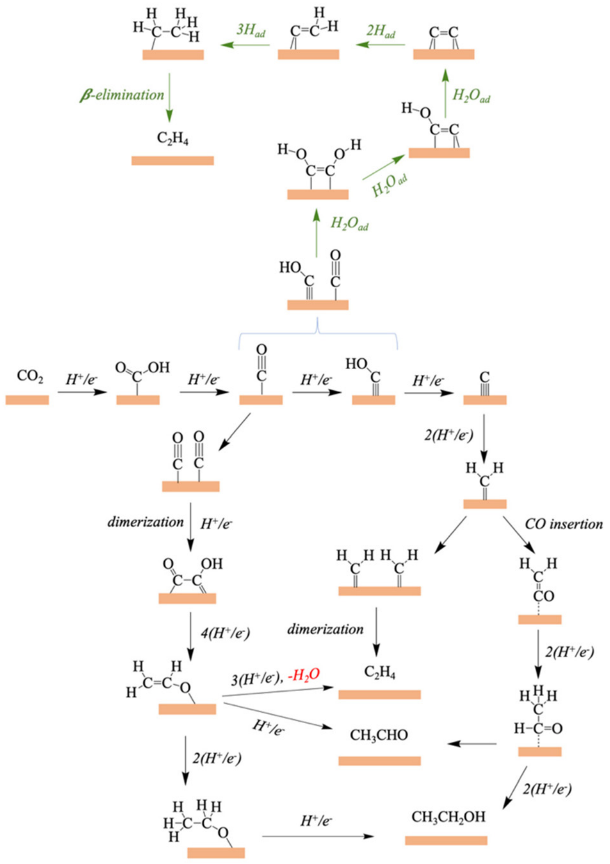

Fig. 4 Illustration of eCO_2RR pathways for the formation of C_2H_4, CH_3CHO and C_2H_5OH.

As noted above, extensive eCO_2RR studies with many metals in the periodic table have revealed that Cu has the unique capability of producing an extensive range of reduced carbon products containing one carbon (C_1), two carbons (C_2) or multi-carbons (*i.e.* more than two carbons; C_{2+}). The 16 products detected using Cu catalysts during eCO_2RR and their structures are shown in Fig. 5.[38–41] This on one hand demon-

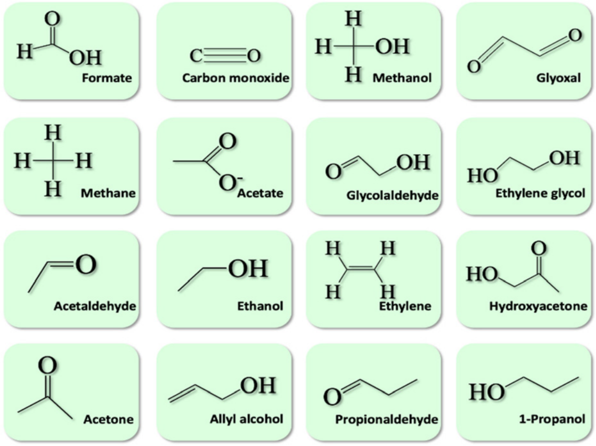

Fig. 5 Graphical representation of products detected during eCO_2RR at a Cu electrode. Adopted and redrawn.[38]

strates the versatility of Cu catalysts, but on the other hand implies that poor product selectivity is a major challenge to address for commercial applications.

In attempts to address the selectivity issue, nanostructuring, alloying, defect engineering, atomizing, and the synthesis of oxide, sulphide, and nitride-derived Cu as well as other methods have been employed.[17,21,42–49]

Since alloying is one of the most promising and fundamental strategies for manipulating the reaction pathways to obtain desired products, this review focuses on what has been achieved to date and what might be accomplished in the future by alloying Cu with other eCO_2RR active metals. Several review articles[17,25,50–54] have been published on the use of alloyed-Cu catalysts. However, they focus on a much broader aspect of eCO_2RR with copper. In this review, the correlation between alloy type and selectivity is examined and future directions in the development of Cu based alloys as effective eCO_2RR catalysts are proposed. Finally, in order to provide an overview of the status of findings with alloyed-Cu catalysts, comparisons of what has been achieved with state-of-the-art Cu alloys and other Cu based catalysts for each eCO_2RR product also are provided in a table at the end of each section.

2. Catalyst performance descriptors

The effectiveness of eCO_2RR is determined by the following descriptors:

(a) Faradaic efficiency: faradaic efficiency (FE) is the indicator of the selectivity of the products obtained with a catalyst during eCO_2RR. FE (reported in %) is calculated by using the formula given in eqn (1)

$$\mathrm{FE}\,(\%) = \frac{nNF}{Q} \times 100 \tag{1}$$

where N represents the number of moles of the product formed, n is the number of electrons transferred for the formation of one molecule of the product, F is the Faraday constant (96 485 C mol^{-1}) and Q is the amount of charge passed during electrolysis.

(b) Overpotential: overpotential (η) is the difference between the applied potential (E_{applied}) to obtain a product and the equilibrium potential ($E^{\circ\prime}$). It is calculated by using the formula given in eqn (2)

$$\eta = |E_{\text{applied}} - E^{\circ\prime}|. \tag{2}$$

(c) Current density: current density (j) denotes the rate/s of electrochemical reaction/s. It is the catalytic current (i) generated per unit area. Current densities presented in many studies are calculated with respect to the geometric area of the electrode. However, ideally an electrochemical active surface area should be used. Partial current density (j_{product}) indicates the rate of formation of a given product and calculated by the formulae given in eqn (3) and (4)

$$j_{\text{total}} = \frac{i_{\text{total}}(\text{mA})}{\text{area}(\text{cm}^2)} \tag{3}$$

$$j_{\text{product}} = j_{\text{total}} \times \mathrm{FE}_{\text{product}} \tag{4}$$

(d) Stability: the stability is the lifetime of a catalyst for performing eCO_2RR. In general, it is the time period for which a catalyst provides stable activity and selectivity.

3. Strategies for alloying copper

Watanabe *et al.*,[55] were the first to report eCO_2RR on Cu alloys formed by electroplating. They found that alloy catalysts often exhibited distinctly different catalytic properties from their constituent elemental metals. This feature was later attributed to electronic and geometric effects at the catalyst surface that arise due to alloying.[17,36,50,56] The electronic effect is generated in an alloy due to the interaction between the constituent elemental metals with different electronic properties and/or the lattice mismatch between two adjacent metals, which alters the binding strength of the eCO_2RR intermediates. The geometric effect arises from the change in the arrangement of the alloyed metals in the catalyst which alters the environment near the active sites for the eCO_2RR intermediates and hence impacts their binding and subsequent reactions.

The structure of the alloy or in other words, its atomic arrangement play a crucial role in determining the selectivity of the products formed during eCO_2RR. Alloy systems can be ordered, intermetallic, disordered, core/shell structured, phase-separated and have high entropy structures (Fig. 6(a)). All these variations have been explored in the design of catalysts for eCO_2RR. Intermetallic alloy systems having an ordered atomic arrangement are the most stable form of alloys. With thermodynamically stable alloy forms, the electronic structure and atomic co-ordination environment can be controlled precisely as they possess a specific crystal structure.[57] By altering the alloy composition, bond lengths can be tuned, which effects the binding energies of molecules adsorbed on the surface of the catalysts and hence their catalytic behaviour.

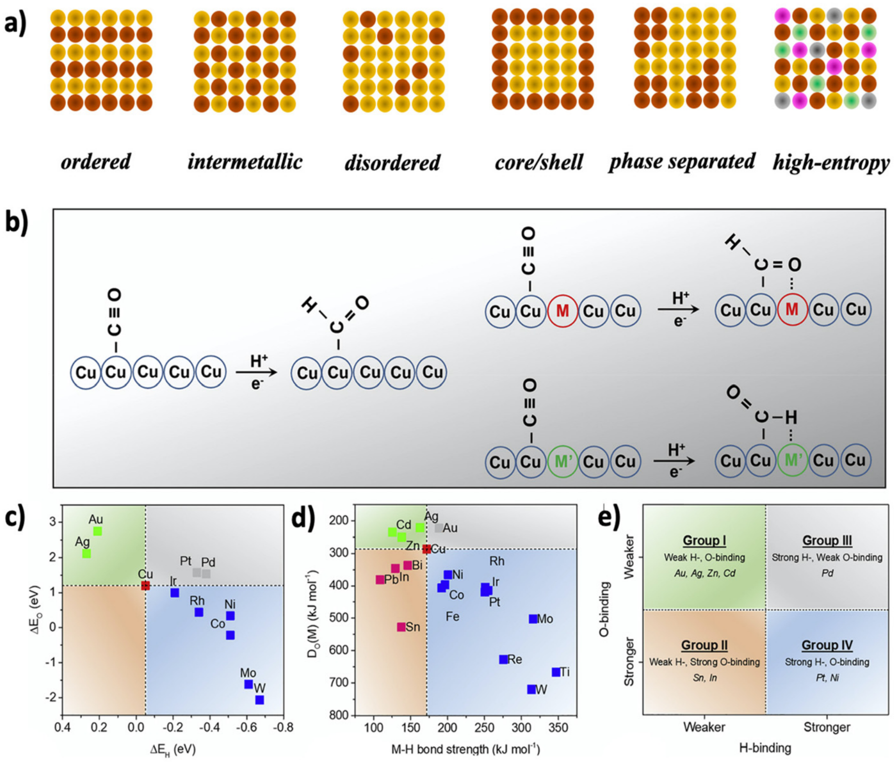

Fig. 6 (a) Alloy systems reported in the literature. (b) Illustration of binding of eCO$_2$RR intermediates to Cu, Cu–M and Cu–M′ alloy catalysts where M is the guest metal with O-affinity and M′ is the guest metal with H-affinity, (c) H and O binding energies for designated metals, (d) M–H bond strength shown as a function of bond dissociation enthalpy of metal oxides, (e) classification of metals into different groups with respect to Cu, based on their O and H affinities. Reprinted with permission.[25] Copyright 2018, Elsevier Inc.

Disordered alloys are solid-solution mixtures with irregular arrangements of binary atoms. They are generally thermodynamically unstable and their local electronic and the geometry of their structures often changes during the electrolysis process.[57,58]

The catalytic properties in core/shell structured alloys are regulated by the strain and ligand effects that arise between the core and shell materials. Strain effects such as tensile stress on the surface of atoms arise due to the lattice mismatch between core/shell interface.[59,60] Ligand effects are short-range and only exist within two or three atomic layers from the surface.[61] Atomic vacancies and metal doping in the shell material also can occur. They are a function of the thickness of the shell and also impact on the product selectivity during electrolysis.[62] In eCO$_2$RR, the major benefit of such alloys is the creation of phase interfaces where the products formed at one phase can migrate through the interface and be further reduced to C$_{2+}$ products. These catalytic Cu alloy forms are being extensively studied as a means of increasing the CO environment at Cu and facilitating the production of highly reduced C$_{2+}$ products such as ethylene and ethanol.[63–65] Details of the efficiency of phase separated alloy catalysts and the CO spill-over effect are discussed below.

High entropy alloys (HEAs) are a novel class of alloys recently being investigated for eCO$_2$RR. These alloys are formed by about five metals, with each element constituting between 5–35% and with variation in the elemental ratios. Accordingly, a large variety of elemental combinations is possible in the alloy and consequently a wide range of catalytic capabilities can be achieved.[66,67]

Compared to bimetallic alloys, HEAs provide superior stability and durability particularly under harsh reaction conditions such as high temperature and high electrochemical potential due to their high mixing entropy and hence low Gibbs free energy as quantified by eqn (5).[67,68]

$$\Delta G_{\text{mix}} = \Delta H_{\text{mix}} - T\Delta S_{\text{mix}} \tag{5}$$

where ΔG_{mix} is the change in the Gibbs free energy of the alloy system, ΔS_{mix} is the change in the entropy of the alloy system, ΔH_{mix} is the change in the enthalpy of the alloy system, and T is the temperature. In addition, the random atomic arrangement in the lattice leads to variation in lattice potential energy at different locations which provides a higher diffusion activation energy that contributes to the stability of the alloy.[69] Furthermore, due to lattice distortion effects resulting from the presence of multiple elements, HEAs have more flexibility to alter their chemical and physical properties.[67,70,71] In terms of electrolysis, this effect helps the optimization of the coordination environment of atoms on the catalyst surface as well as the adsorption and desorption energies of key reaction intermediates.[68] Similar to the synergistic effects in bimetallic alloys, HEAs possess a “cocktail effect” resulting from the interactions between multiple elements. As a result of a range of novel features, these alloys offer new properties with respect to corrosion and oxidation resistance, and other mechanical properties.[68,70] The unique characteristics of HEAs change the scaling relationships and provide a wide window of opportunity for manipulating the reaction pathways and overcoming the limitations of conventional alloys.[72]

Grouping of metals according to their binding affinities for *H and *O relative to copper was proposed to facilitate the selection of a guest metal to form a binary alloy with Cu.[25] In the alloy, the bimetallic catalyst material will have two binding sites available to achieve stabilisation of a desired intermediate. For example, metals which produce hydrogen have a more robust *H and *O affinity than Cu while those with weaker *O and *H binding strengths, produce CO *via* a *COOH intermediate. Metals having a lower H affinity but higher O-affinity than Cu favour formation of the *OCHO intermediate, which leads to formation of formate. Hence, metals with good O-affinity can be alloyed with Cu to stabilize O-bound intermediates, while those having H-affinity can stabilize H binding in the intermediates, as illustrated in Fig. 6(b). Fig. 6 (c–e) show a comparison of O and H affinities of some metals with respect to copper and the grouping of metals. In the following sections, the factors that govern the selectivity of Cu alloy towards each product are summarized and discussed to guide the development of advanced alloy catalysts. Examples of the state-of-the-art Cu alloys and other Cu based catalysts for each product are also given.

4. Copper alloys for selective reduction of CO_2

4.1 Formate and CO

4.1.1 Formate. Catalysts obtained by alloying Cu with formate favouring metals, such as Bi,[74–78] Sn,[79–83] Pb,[84–88] Pd,[89–93] Mo[94] and Sb,[95–97] particularly as intermetallics, composites and surface alloys, often produces formate with good efficiency.[98,99]

Copper modified with Pd and Pd–H produces significant amounts of formate. For example, early studies by Fujishima and co-workers showed substantial formate production at the Pd modified Cu electrodes.[100,101] Zhang *et al.*[102] have synthesised a stannate derived Sn–Cu bimetallic catalyst *via* cation exchange with $Na_2Sn(OH)_6$ followed by annealing and electroreduction. This Cu–Sn catalyst produced 86% formate at −1.1 V *vs.* RHE in 0.5 M $NaHCO_3$ with a partial current density of ∼11 mA cm^{-2}. These authors also reported that a slight increase in formate faradaic efficiency could be achieved by incorporating the Cu–Sn catalyst into reduced graphene oxide along with a major increase in partial current density. The Hod group[103] reported the favorable formation of formate with 3D structured Cu_2S catalysts prepared by an electrochemically driven cation exchange mechanism. To prepare such electrodes, pre-synthesised CoS_x nanosheets based 3D structures were taken as templates and a cation exchange reaction with Cu^{2+} (where Co^{2+} ions in CoS_2 were replaced with $Cu^{1+/2+}$ ions) was performed electrochemically in a 0.1 M $LiClO_4$-dimethylformamide electrolyte solution containing 3 mM $Cu(NO_3)_2$ by applying a potential of −0.47 V *vs.* normal hydrogen electrode for varied time periods. The amount of Co^{2+} replaced with Cu^{2+} ions was varied by controlling the charge passed during the electrochemical reaction. The formate production was found to be somewhat dependent on the percentage of Co^{2+} ions exchanged by Cu^{2+}. With a Cu_2S sample obtained by passing 2.0 C of charge, 87.3% of formate was produced with a partial current density of 19 mA cm^{-2} at −0.9 V *vs.* RHE in 0.1 M $NaHCO_3$ solution saturated with CO_2. The authors reported that variation of the grain boundary obtained with the modulation of binary cations was the origin of the change in the product selectivity.

Ag is an excellent CO formation catalyst.[104] However, AgCu alloy can be designed to favour formate formation. Recent work on CuAg bimetallic nanoarchitectures demonstrated the importance of electronic and geometric modulation of the catalyst with respect to product selectivity.[73] The sponge-like $Ag_{91}Cu_9$ and coralline $Ag_{65}Cu_{35}$ nanoalloys prepared by anodising $Ag_{52}Cu_{39}Sn_9$ alloy foil induced a dramatic change in the selectivity of CO *versus* HCOOH. Changing the composition of the AgCu alloy, modifies the electronic arrangement of Ag and Cu and hence the binding strengths of intermediates as demonstrated by *in situ* Raman spectroscopic measurements shown in Fig. 7. Thus, on increasing the Cu content of the AgCu alloy, the selectivity shifted from favouring CO to forming formate with a faradaic efficiency of 96%.

Table 2 provides details of some state-of-the-art Cu alloys and other Cu based catalysts for selective formate production.

4.1.2 CO. Metals such as Zn,[105–109] Ag,[110–114] Au,[115–119] Pd,[89,120–123] which are highly selective for CO, have been alloyed with copper to enhance CO production in many studies. Post-transition metal such as In[124–128] and Sn[129–133] that are selective for formate generation also have been com-

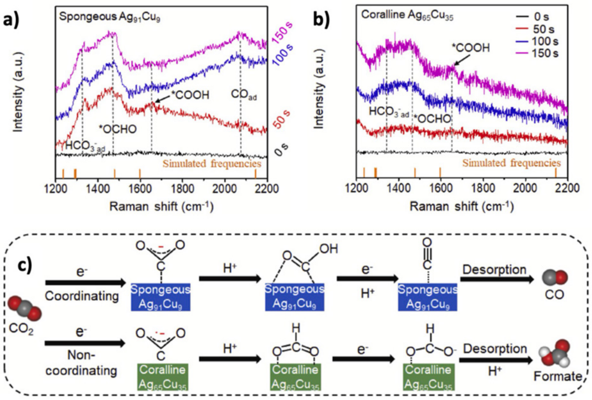

Fig. 7 (a and b) *In situ* Raman spectra obtained during electrolysis and (c) proposed reaction pathways on spongeous $Ag_{91}Cu_9$ and coralline $Ag_{65}Cu_{35}$ alloy nanoarchitectures. Reprinted with permission.[73] Copyright 2020, Elsevier Ltd.

Table 2 Examples of formate production with state-of-the-art Cu alloys and other Cu based catalysts

Catalyst	Electrolysis cell	Electrolyte	Potential (V *vs* RHE)[a]	FE (%)	j_{HCOO^-} (mA cm^{-2})	Ref.
Cu–Sn/rGO	H-cell	0. 5M $NaHCO_3$	−1.0	87.4	20.7	102
Cu_2S-2.0C	H-cell	0.1 M $NaHCO_3$	−0.9	87.3	19.1	103
Coralline $Ag_{65}Cu_{35}$	H-cell	0.1 M $KHCO_3$	−1.0	91.8	16.8	73
CuCd@Cu-20,45	H-cell	0.5 M $NaHCO_3$	−1.1	70.1	26.8	99
Porous $Cu_{6.26}Sn_5$	H-cell	0.1 M $KHCO_3$	−1.1	97.8	~30	136
CuBi-100	H-cell	0.5 M $KHCO_3$	−1.0	94.7	13	137
Cu/Au	H-cell	0.5 M $KHCO_3$	−0.6	81	10.4	138
Sn–Cu	H-cell	0.1 M $KHCO_3$	−0.95	92	~10	139
Cu@Sn nanocones	H-cell	0.1 M $KHCO_3$ + 0.3 M KCl	−1.1	90.4	52	140
CuSn alloy@Cu doped SnO	H-cell	0.5 M $KHCO_3$	−1.2	95.4	30.3	141
$C_{11.5}In_{88.5}$-OH	H-cell	0.1 M $KHCO_3$	−1.1	85	~10	142
MOF derived CuBi	H-cell	0.5 M $KHCO_3$	−0.77	100	67.9	143
Cu_2O/CuO/CuS	H-cell	0.1 M $KHCO_3$	−0.7	84	20	144
CuBi NPs	H-cell	0.1 M $KHCO_3$	−0.99	96	12.5	145
CuS	H-cell	0.1 M $KHCO_3$	−0.8	80	18	146
HCS/Cu-0.12	H-cell	0.5 M $KHCO_3$	−0.81	82.4	26	147
S-doped OD-Cu	H-cell	0.1 M $KHCO_3$	−0.8	73.6	13.9	148
Cu_6Sn_5/Sn	Flow cell	1 M KOH	−1.0	86.7	103	149
CuSn/Sn	Flow cell	1 M $KHCO_3$	−0.7	84.2	~26	150
CuBi	MEA	0.5 M $KHCO_3$	−1.07	98.3	55.6	151

[a] Potential at which maximum FE was obtained.

bined with copper to tune the selectivity towards CO. This was achieved by alloying copper with metals where in most of the cases, at least one of the following situations exists: the alloy possesses (i) copper in an oxidized form, (ii) a lattice mismatch between the copper phase and the guest metal phase, (iii) a higher shared boundary between the copper and guest metal phases. Consequently, synergistic geometric and electronic effects emerge which influence product formation. Various factors influencing the CO selectivity over the copper-based bimetallic alloys are discussed below.

In early studies in the 1990s, Watanabe *et al.*[55,134] prepared CuZn alloys electrodes by electroplating onto gold electrodes and studied the eCO$_2$RR efficiency in 0.05 M $KHCO_3$ electrolyte. They reported that higher concentrations of Zn in the CuZn alloy led to an increase in CO generation compared to the use of pure Cu. The only other eCO$_2$RR product found was $HCOO^-$. The Berlinguette group[135] studied eCO$_2$RR using brass and bronze catalysts. They prepared 21 catalysts with varying Cu : Zn : Sn ratios by drop casting methanolic solutions of Cu, Zn, and/or Sn in the required proportions onto a titanium substrate followed by multiple exposures to near-infrared radiation and electroreduction to produce alloy films. Four-hour eCO$_2$RR experiments with these film electrodes generated H_2, CO and HCOOH as products. Cu–Zn–Sn alloys with Sn < 20% generated mainly syngas with the H_2 : CO ratio depending on the ratio between Cu and Zn. Hu *et al.*[152] prepared Cu–Zn catalysts by annealing a brass substrate at 500 °C in an Ar atmosphere prior to electroreduction of ZnO formed in the Zn metal annealing step, as shown in Fig. 8(a). On annealing, uniform 200 nm particles formed over the brass substrate. Zn and Cu have different melting points of 419.5 °C and 1085 °C, respectively. Accordingly, Zn melts at 500 °C and migrates all over the surface and is then converted to ZnO on exposure to air while Cu remains unchanged. The resultant catalyst used for eCO$_2$RR over a range of applied potentials produced syngas with a 2 : 1 ratio of CO : H_2 (Fig. 8(b)) which is suitable for the Fischer–Tropsch process. The Broekmann group[153] synthesised $Zn_{94}Cu_6$ alloy foams, as displayed in Fig. 8(c and d), by dynamic hydrogen bubble template assisted electrodeposition onto a Cu plate. eCO$_2$RR with this catalyst produced 90% CO at −0.95 V *vs.* RHE in aqueous 0.5 M $KHCO_3$ electrolyte

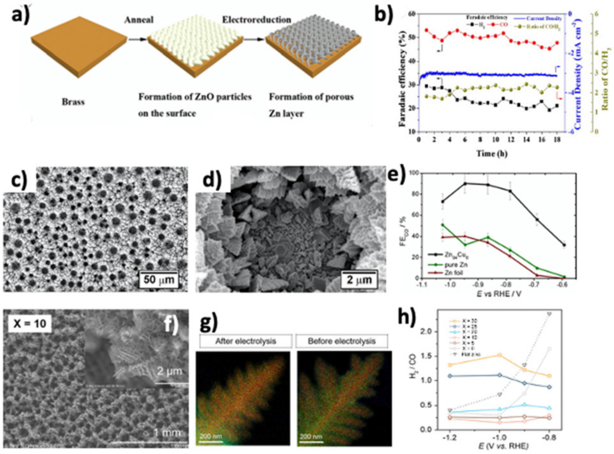

Fig. 8 (a) Schematic illustration of the preparation of Zn–Cu catalysts from brass foil, (b) faradaic efficiencies, current density and CO/H_2 ratio obtained during eCO2RR as a function of time. Reprinted with permission.[152] Copyright 2018, Elsevier B.V. (c and d) SEM images of the $Zn_{94}Cu_6$ catalyst, (e) CO faradaic efficiencies obtained with designated CuZn and Zn catalysts. Reprinted with permission.[153] Copyright 2018, the American Chemical Society. (f) SEM, (g) scanning transmission electron microscope – energy-dispersive X-ray spectroscopy (STEM-EDXS) mapping images of $Zn_{90}Cu_{10}$ catalyst (h) ratio of H_2/CO faradaic efficiencies obtained with designated $Zn_{100-x}Cu_x$ catalysts. Reprinted with permission.[154] Copyright 2019, Wiley-VCH Verlag GmbH & Co. KGaA, Weinheim.

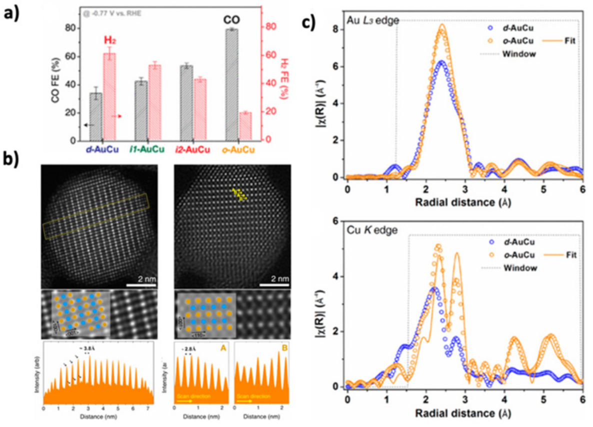

Fig. 9 (a) Faradaic efficiencies for generation of H_2 and CO using AuCu alloy nanopartcles with designated atomic ordering, (b) high-angle annular dark-field imaging – scanning transmission electron microscope (HAADF – STEM) analysis of ordered AuCu nanoparticles, and (c) XAS analysis of ordered and disordered AuCu nanoparticles. Reprinted with permission.[157] Copyright 2017, the American Chemical Society.

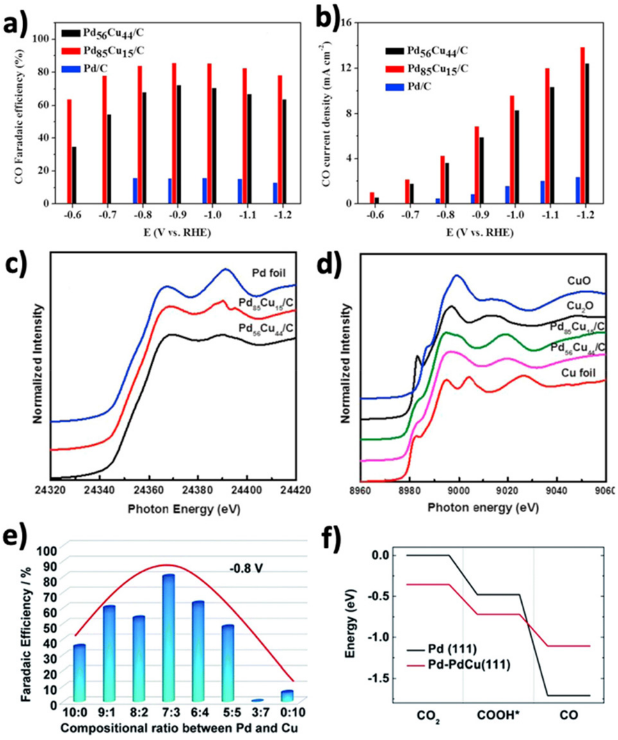

Fig. 10 (a) CO faradaic efficiency Pd_xCu_y nanoparticles, (b) CO partial current densities obtained using designated Pd_xCu_y nanoparticles. (c) Pd K edge, and (d) Cu K edge XANES spectrum of a PdCu/C catalyst. Reprinted with permission.[158] Copyright 2016, Elsevier Ltd. (e) A comparison of CO selectivity at PdCu NPs with specified compositions, (f) free energy diagram for CO_2, *COOH and CO on a Pd terminated PdCu (111) surface. Reprinted with permission.[159] Copyright 2016, the Royal Society of Chemistry.

(Fig. 8(e)). Lamaison *et al.*[154] also designed Cu–Zn alloy foam catalysts by electrodeposition of Cu onto Zn plates in their eCO_2RR application. These foams were composed of a dendritic CuZn alloy structure (Fig. 8(f and g). As shown in Fig. 8(h), bulk electrolysis experiments performed under eCO_2RR conditions with 0.1 M $CsHCO_3$ as the electrolyte revealed an increase in the $H_2 : CO$ ratio with increasing Cu content.

CuAu alloys, like CuZn ones, have been extensively studied for eCO_2RR generation of CO. For example, enhancement of CO at Au_xCu_{100-x} alloy catalysts has been reported by Christophe *et al.*[155] In particular, a significant increase in the production of CO was observed with use of an $Au_{50}Cu_{50}$ catalyst. CO desorption at Au sites is promoted by the presence of adsorbed CO on Cu sites due to dipole repulsion between CO molecules at adjacent sites. Consequently, the presence of both Cu and Au in an optimal ratio enhances CO product formation. Bimetallic AuCu catalysts also induce an electronic effect which results in the shift in the d-band centre and hence changes the binding strength of the reaction intermediates. As a result of the shift in the d-band centre, the way the metals in the AuCu alloy interact with adsorbed intermediate also changes. The implication of this feature was examined by Kim *et al.*[156] who found that the evolution of CO increases with increasing Au content in the AuCu alloy. In the case of Au_3Cu, they reported a mass activity (*i.e.* current density normlised to the amount of catalyst loaded) exceeding 200 A g^{-1} at −0.73 V *versus* RHE, which represents a ten-fold increase in comparison with pure Cu. Surface valence band photoemission spectral analysis suggested that the improved selectivity towards CO with Au_3Cu could also be due to the synergistic electronic and geometric effects associated with AuCu nanoparticle formation that occurred during the eCO_2RR. The atomic arrangement of Au and Cu in AuCu bimetallic alloy nanoparticles (either ordered or disordered) also can have an impact. Among AuCu alloy nanoparticles, the nanoparticles with an ordered arrangement of Au and Cu (o-AuCu) exhibited a factor of two improvement in selectivity for CO (Fig. 9(a)).[157] STEM (Fig. 9(b)) and X-ray absorption spectroscopy (XAS) (Fig. 9(c)) analyses revealed that a thin layer of segregated Au atoms was formed on the surface of o-AuCu nanoparticles during electrolysis. DFT calculations suggested that the lattice strain of 6% associated with the Au layer due to the underlying AuCu lattice affected the catalytic activity of o-AuCu nanoparticles.

Intermetallic CuPd alloy catalysts provide another example of a Cu alloy that enhances CO generation during the eCO_2RR process.[159–161] Excellent selectivity for CO with a faradaic efficiency of 86% and a partial current density of 6.9 mA cm^{-2} was obtained on $Pd_{85}Cu_{15}$ alloy nanoparticles (Fig. 10(a and b)).[158] On increasing the Cu content in the alloy, the efficiency decreased. X-ray absorption near edge structure (XANES) analysis shown in Fig. 10(c and d) for the PdCu alloy nanoparticles revealed that variation in Pd–Pd and Cu–Cu bond lengths alters the binding strengths of the CO_2 reduction intermediate (*CO). Further, the formation of Pd and Cu oxides at higher Cu to Pd ratios leads to suppression of CO evolution during electrolysis. CuPd alloys with a 1.5 : 8.5 atomic ratio bind CO less strongly on the surface than with pure Pd, resulting in an enhancement of CO production.

The study by Li *et al.*[159] with mesoporous CuPd alloys also shows composition-dependent activity for CO_2 conversion (Fig. 10(e)). An alloy with a Cu to Pd ratio of 3 : 7 gives high CO yields, which diminishes with an increase in the Cu content. DFT calculations predict that Pd terminated Pd_7Cu_3 alloy surfaces faceted with (111) planes will favour adsorption of a *COOH intermediate and weaken adsorption ability of *CO resulting in excellent CO selectivity (Fig. 10(f)). Due to the differences in electronegativity of Cu and Pd, the presence of Cu atoms adjacent to Pd in a Cu–Pd alloy increases the adsorption of *COOH and CO on Pd surfaces, making Pd sites the active sites for the eCO_2RR.

Oxide derived Cu–M (M = In/Sn) catalysts have been surveyed for their ability to convert CO_2 to CO. In and Sn in their metallic,[162] oxide[163–165] or chalcogenide[166–168] forms produce $HCOO^-$ from the eCO_2RR. However, when oxides of these post-transition metals are combined with copper, scaling relationships can be altered due to synergistic effects associated with the lattice mismatch between Cu/CuO and MO_2 (M = In/Sn). The result is that product selectivity is shifted from formate to CO with remarkably high faradaic efficiencies. For example, the study by Li *et al.*,[169] shows that the change in product distribution as a function of the thickness of the SnO_2 coated onto Cu nanoparticles (Fig. 11(b and c)). With a thin SnO_2 shell (0.8 nm), the product selectivity for CO had a FE of >90% at −0.6 V *vs.* RHE with little formate produced. In contrast, with a thick SnO_2 shell (1.8 nm), the eCO_2RR behaviour is similar to that at Sn and formate is the major product. According to the results of DFT calculations, the synergistic effect emerged because of the compression strain and self-doping of Cu into the thinner SnO_2 shell layer during electrolysis which shifted selectivity from $HCOO^-$ to CO. A related study using Cu–In_2O_3 core–shell nanoparticles (Fig. 11(d))[170] also showed that the thinnest shell provided a shift in selectivity to CO (Fig. 11(e and f)). With the thinner In_2O_3 shell, the lattice mismatch between Cu and In_2O_3 facilitates self-doping of Cu into the In_2O_3 shell resulting in alteration of binding energies of *COOH and *OCHO intermediates, which leads to the generation of CO and HCOOH, respectively. Cu oxide surfaces decorated with Sn also enhance conversion of CO_2 to CO.

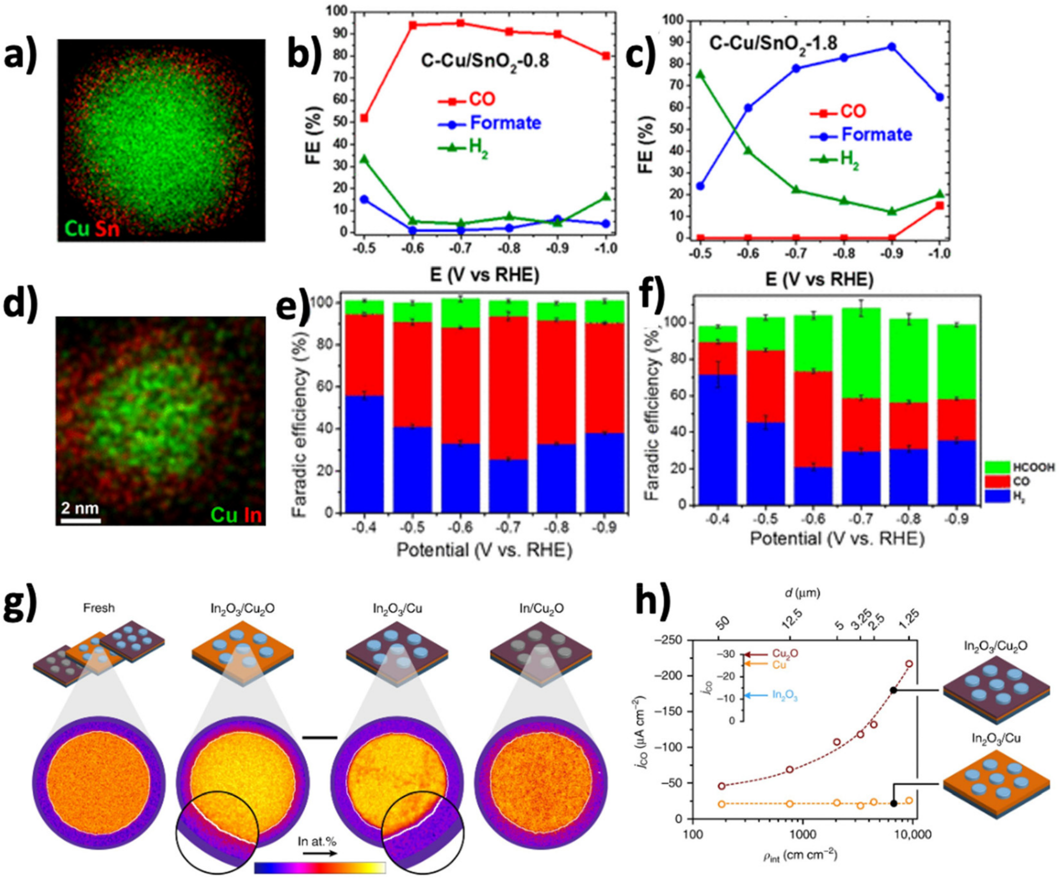

Fig. 11 (a) Electron energy loss spectroscopy (EELS) elemental mapping of Cu/SnO_2 nanoparticles. (b) and (c) faradaic efficiencies of products obtained during eCO_2RR with Cu/SnO_2 NPs having a shell thickness of (b) 0.8 nm and (c) 1.8 nm. Reprinted with permission.[169] Copyright 2017, the American Chemical Society. (d) EDS elemental mapping of C–Cu/In_2O_3 nanoparticles. (e) and (f) faradaic efficiencies of products obtained during eCO_2RR with Cu/In_2O_3 nanoparticles having a shell thickness of (e) 0.4 nm and (f) 1.5 nm. Reprinted with permission.[170] Copyright 2018, the American Chemical Society. (g) elemental mapping showing the formation of indium islands when undertaking eCO_2RR with CuIn electrodes, (h) CO partial current density obtained during eCO_2RR at −0.6 V with In_2O_3/Cu_2O and In_2O_3/Cu electrodes as a function of island diameter and interfacial density. Reprinted with permission.[171] Copyright 2018, Nature Publishing Group.

Zhao *et al.*[172] decorated electrochemically generated CuO nanowires with Sn. An optimal loading of Sn produced 90% of CO at −0.8 V *vs.* RHE in 0.1M $KHCO_3$ electrolyte. Sarfraz *et al.*[173] electrochemically deposited Sn on a Cu sheet. With a Sn loading of 3.9 mol cm^{-2}, 90% of CO was obtained at −0.6 V *vs.* RHE in 0.1 M $KHCO_3$. However, with higher Sn loadings, selectivity reverted to $HCOO^-$. Zeng *et al.*[174] used Cu–Sn foam based dendritic structures, where the Cu dendrites were decorated with small amounts of SnO_x to form a Cu/CuO_x–SnO_x core/shell structure. This allowed 93–94% CO to be formed between −0.75 V and −0.9 V *vs.* RHE in 0.1 M $KHCO_3$.

Studies by the Takanabe group[175,176] employing In coated on oxide derived (OD)-Cu[175] and $CuInO_2$ derived Cu–In alloy[176] catalysts again revealed a drastic increase in CO selectivity. DFT calculations suggest that the replacement of a Cu atom with an In atom would suppress *H adsorption with *CO adsorption energy unchanged, resulting an increase in the FE of CO while decreasing HER. A study by Larrazábal *et al.*[177] proposed that an *in situ* generated metastable $In(OH)_3$ phase in the oxide plays an important role in the use of Cu–In catalysts. The core–shell structured Cu–In catalysts, with $In(OH)_3$ as the shell evolved upon repeated voltammetric cycles of potential on the initial Cu–In in a 0.1 M $KHCO_3$ solution, exhibited a significant increase in the CO selectivity. The same group also reported the dependence of CO selectivity on the nature of the Cu–In interfaces.[171] In their study, the authors microfabricated In_2O_3 dots on Cu and Cu_2O surfaces. In_2O_3 dots on Cu left the selectivity unaltered, whereas those on Cu_2O led to a drastic improvement in selectivity for CO. When the interfacial density is low, both catalysts showed similar activity. However, when the density of metal–oxide interface was increased, the catalytic activity towards CO was enhanced with In_2O_3/Cu_2O, as shown in Fig. 11(h). The irregular layer of Cu formed by reduction of Cu_2O enhances the diffusion of In (Fig. 11(g)) giving rise to a synergistic effect at Cu–In interfaces. This study reveals that both the interfaces and Cu_2O are essential for achieving synergistic effects that tune the selectivity pathway.

State of the art Cu alloys and other Cu based catalysts that favoured CO production are tabulated in Table 3.

4.2 Highly reduced C_1 products

4.2.1 Methane. The formation of methane on Cu based bimetallic catalysts with the eCO_2RR was reported in early literature using Cu modified Pd and PdH catalysts.[100,101] The amount of hydrogen absorbed in PdH has a significant effect on the selectivity for methane. For instance, the methane production was enhanced initially at Cu–PdH catalysts with lower coverages of adsorbed H on Pd. However, there was no further increase in CH_4 at higher concentrations of adsorbed H.

Electrochemical conversion of CO_2 to methane has been explored on Cu–Zn catalysts. Cuenya and co-workers[184] studied the eCO_2RR product selectivity dependence on the composition and structure of CuZn nanoparticles derived from adoption of the inverse micelle encapsulation method. Their bulk electrolysis eCO_2RR experiments with $Cu_{100-x}Zn_x$ revealed the presence of Zn from 10% to 50% increased CH_4 formation while higher 50% Zn levels suppressed CH_4 formation and increased that of CO (Fig. 12(a)). The XANES studies suggested that the Cu–ZnO interface is needed to generate CH_4 or other hydrocarbons while CuZn (brass) alloy favours formation of CO/H_2 mixtures. Due to the faster reduction rate with CuO than with ZnO, in samples with a lower Zn content ($Cu_{100-x}Zn_x$, $x < 50$), the Cu–ZnO interface prevailed in the initial period of time during eCO_2RR, when the hydrogenation of CO species was favoured at Cu sites. When both oxides were fully reduced, brass nanoparticles were generated so that Cu loses its ability to stabilise $*CH_y$ (y = 1–3) intermediates due to ligand effects and hence CO and H_2 were released as the electrolysis products.

Ceria (CeO_2) is another material that facilitates CH_4 production in the presence of Cu sites during eCO_2RR.[185] Doping CeO_2 nanorods with Cu establishes a strong interaction between atomically dispersed Cu sites and CeO_2. Accordingly, multiple oxygen vacancies are induced around Ce under eCO_2RR conditions, which provides an effective site for electro-

Table 3 Examples of the state-of-the-art Cu alloys and other Cu based catalysts that favour CO production

Catalyst	Electrolysis cell	Electrolyte	Potential (V *vs.* RHE)[a]	FE (%)	j_{CO} (mA cm^{-2})	Ref.
$Zn_{94}Cu_6$ nanofoam	H-cell	0.5 M $KHCO_3$	−0.9	90	~4.5	153
o-AuCu NPs	H-cell	0.1 M $KHCO_3$	−0.8	~80	1.4	157
Mesoporous Pd_7Cu_3	H-cell	0.1 M $KHCO_3$	−0.8	80	~1.5	159
$Pd_{85}Cu_{15}/C$	H-cell	0.1 M $KHCO_3$	−0.9	86	6.9	158
C–Cu/SnO_2-0.8	H-cell	0.5 M $KHCO_3$	−0.7	93	~13	169
Cu–Sn10 nanowires	H-cell	0.1 M $KHCO_3$	−0.8	90	4.5	172
Cu–Sn	H-cell	0.1 M $KHCO_3$	−0.6	90	1.0	173
Cu–Sn foam	H-cell	0.1 M $KHCO_3$	−0.8	94	3	174
PTFE-Cu	H-cell	0.1 M $KHCO_3$	−0.4	71	1.5	178
Cu NPs-700	H-cell	0.1 M $KHCO_3$	−0.6	75.6	3.8	179
Cu–N_2/GN	H-cell	0.1 M $KHCO_3$	−0.5	81	~2	180
Cu/CNT	PEM Cell[b]	0.1 M $KHCO_3$	−3.5[c]	75.7	12.2	181
CuPd nanosheets	Flow cell	1 M KOH	−0.6	71	58	161
2.7 nm PdCu NPs	Flow cell	1 M KOH	−1.0	82	80	182
Sb–Cu_2O	Flow cell	0.1 M KOH	−0.8	96	60	183

[a] Potential at which maximum FE was obtained. [b] Polymer electrolyte membrane electrolysis cell. [c] Cell voltage.

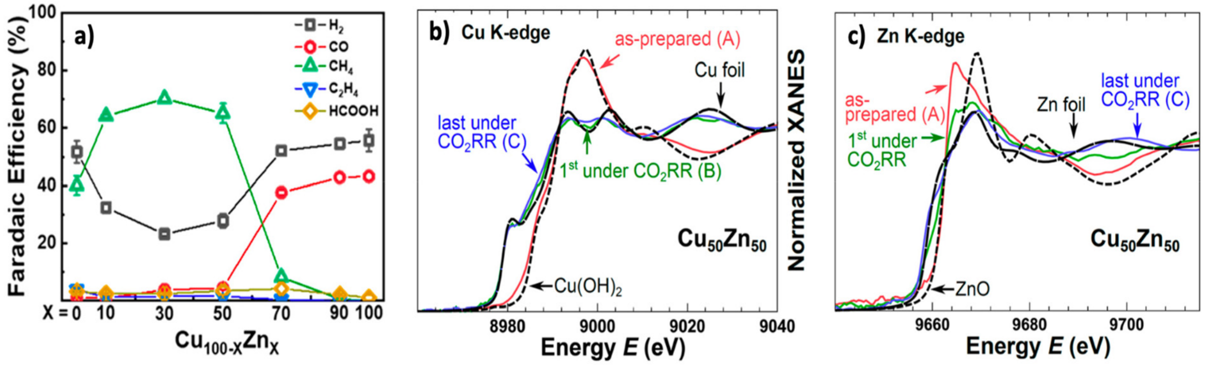

Fig. 12 (a) A comparison of faradaic efficiencies for the products obtained by eCO$_2$RR with Cu$_{100-x}$Zn$_x$ catalysts, (b) Cu K-edge and (c)Zn K-edge XANES spectra of Cu$_{50}$Zn$_{50}$ nanoparticles: spectrum A – as-prepared sample, spectrum B – immediately after the onset of eCO$_2$RR and spectrum C – after 7 h of electrolysis. Reprinted with permission.[184] Copyright 2019, the American Chemical Society. Source: https://pubs.acs.org/doi/10.1021/jacs.9b10709. Further permissions related to the material excerpted should be directed to the ACS.

catalytic reduction of CO$_2$ to CH$_4$. CeO$_2$ nanorods doped with 4% Cu produce ~58% of CH$_4$ at −1.8 V *vs.* RHE with a current density of 56 mA cm^{-2} in 0.1 M KHCO$_3$, as shown in Fig. 13(b). The Buonsanti group[186] has explained the importance of the interaction between CeO$_2$ and Cu in facilitating CH$_4$ formation by examining outcomes of the eCO$_2$RR with Cu/CeO$_2$ heterodimer (HD) nanoparticles as well as physical mixtures of Cu and CeO$_2$ nanoparticles. In addition to the presence of CeO$_2$ interactions with Cu nanoparticles described above, the size of the Cu nanoparticles was shown to plays a significant role in the improvement in CH$_4$ selectivity. The 36 nm sized Cu/CeO$_2$ HD nanoparticles enhanced eCO$_2$RR performance over HER and the selectivity achieved for CH$_4$ reached 54% at −1.2 V *vs.* RHE in 0.1 M KHCO$_3$. In contrast, the Cu and CeO$_2$ physical mixture resulted in only <10% of methane. XAS data (Fig. 13(d)) confirmed that during eCO$_2$RR, Ce^{4+} in Cu/CeO$_2$ HD is reduced to Ce^{3+}. On the basis of DFT calculations, the eCO$_2$RR intermediates (*COOH, *CHO, H$_2$CO*, H$_3$CO*) were postulated to be adsorbed onto both Cu and Ce sites with an O-vacancy in order to form CH$_4$. Thus, oxygen vacancies played a crucial role in enhancing methane selectivity.

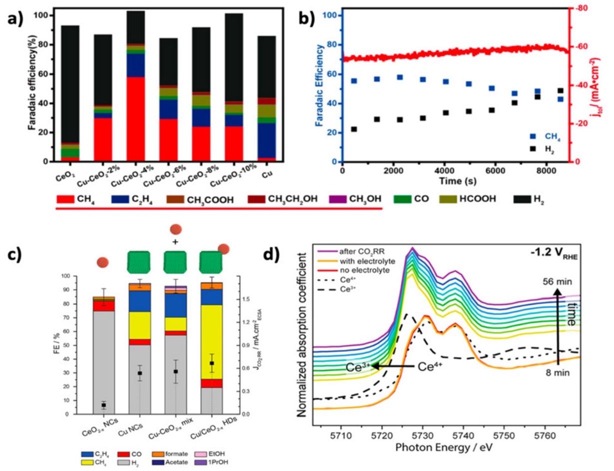

Fig. 13 (a) Comparison of product selectivity obtained with Cu doped CeO$_2$ catalysts, (b) long term stability of a Cu–CeO$_2$-4% (4% of Cu doped in CeO$_2$) catalyst at −1.2 V *vs.* RHE. Reprinted with permission.[185] Copyright 2018, the American Chemical Society. (c) Product selectivity comparison and CO$_2$RR partial current densities obtained with Cu/CeO$_{2-x}$ HDs, Cu–CeO$_{2-x}$ mixture, Cu nanocrystals (NCs), and CeO$_{2-x}$ NCs, (d) Ce L$_{III}$-edge XANES spectra collected every eight minutes when using Cu/CeO$_{2-x}$ HDs under eCO$_2$RR conditions at −1.2 V *vs.* RHE in 0.1 M KHCO$_3$. Reprinted with permission.[186] Copyright 2019, the American Chemical Society.

Chang *et al.*[187] have studied the impact of structural reconstruction of Cu$_{100-x}$Ag$_x$ catalysts on product selectivity using the techniques of *in situ* grazing-angle X-ray scattering/diffraction, X-ray absorption spectroscopy, and Raman spectroscopy. The authors showed that Cu$_{68}$Ag$_{32}$ nanowires underwent dynamic oxidation–reduction cycles on the nanowire surface resulting in an inter diffusion of Ag and Cu atoms prior to stabilization of the metallic states of Cu and Ag. The high methane FE of 60% is three times to that achieved with pristine Cu nanowire.

4.2.2 Methanol.

4.2.2 Methanol. Early studies by Watanabe *et al.*[55,193] on the electrochemical generation of CH$_3$OH by reduction of CO$_2$ used Cu based alloys, particularly CuNi ones. Enhancement of methanol selectivity was reported by Jia *et al.*[194] using a AuCu alloy catalyst deposited electrochemically onto a nanoporous Cu film (NCF). The FE for methanol production was dependent on the alloy composition. With a Cu$_{63.9}$Au$_{36.1}$/NCF catalyst, a FE of 15.9% was achieved which was 19 times higher than with pristine Cu.

Albo *et al.*[195] studied the use of Cu$_2$O/ZnO catalysts for eCO$_2$RR in a flow cell using electrodes prepared by airbrushing commercially available Cu$_2$O and ZnO nanoparticles over carbon paper. They found that the ratio of Cu$_2$O/ZnO has a significant effect on methanol generation during eCO$_2$RR. Cu$_2$O/ZnO with 2 : 1 ratio generated a high selectivity for methanol with a FE of 25.2% at −1.3 V *vs.* Ag/AgCl (sat. KCl) in 0.5 M KHCO$_3$. Recently, Bagchi *et al.*[192] reported excellent selectivity towards methanol could be achieved with an intermetallic

$CuGa_2$ electrocatalyst. An exceptional FE of 77.6% for methanol was achieved at −0.3 V *vs.* RHE. X-ray photoelectron spectroscopy (XPS) and *in situ* X-ray absorption fine structure (XAFS) analysis revealed the importance of surface and subsurface oxides of Ga at low potentials in enhancing methanol selectivity. However, when more negative potentials were applied, lattice expansion occurs, indicating reduction of Ga_2O_3, which resulted in the diminution of methanol selectivity.

Table 4 summarises state-of-the-art Cu alloys and other Cu based catalysts, which are selective for methane and methanol in H type and flow cells.

4.3 C_2/C_{2+} products

C–C coupling is required to produce C_2/C_{2+} products. Electrochemically reducing CO_2 to C_2 products with significant selectivity is a great challenge. Typically, copper is combined with transition metals that generate CO as their primary product during eCO_2RR to improve the selectivity for C_2 products. With Cu–M (M = guest metal) bimetallic alloy catalysts, the formation of C_2 hydrocarbons is impacted by two main effects: the spillover of CO at the boundaries and electronic effects. The geometric arrangement of the Cu and guest metal

Table 4 Examples of the state-of-the-art Cu alloys and other Cu catalysts that favour methane or methanol production

Catalyst	Product	Electrolysis cell	Electrolyte	Potential (V *vs.* RHE)[a]	FE (%)	$j_{product}$ (mA cm^{-2})	Ref.
Cu–ZnO NPs	CH_4	H-cell	0.1 M $KHCO_3$	−1.35	70	∼40	184
4% Cu doped CeO_2	CH_4	H-cell	0.1 M $KHCO_3$	−1.8	58	33.6	185
$Cu_{68}Ag_{32}$ nanowires	CH_4	H-cell	0.5 M $KHCO_3$	−1.2	60	∼27	187
Cu foil	CH_4	H-cell	0.5 M $NaHCO_3$ + methyl carbamate	−2.1	85	31	188
Single atom Cu/GYD	CH_4	H-cell	0.1 M $KHCO_3$	−1.3	66	20	189
Single atom Cu/TCNFs	CH_3OH	H-cell	0.1 M $KHCO_3$	−0.9	44	41	190
Cu (111) nanospheres	CH_4	Flow cell	1 M KOH	−0.91	53	53	191
$CuGa_2$	CH_3OH	Flow cell	1 M KOH	−0.3	78	∼16	192

[a] Potential at which maximum FE was obtained.

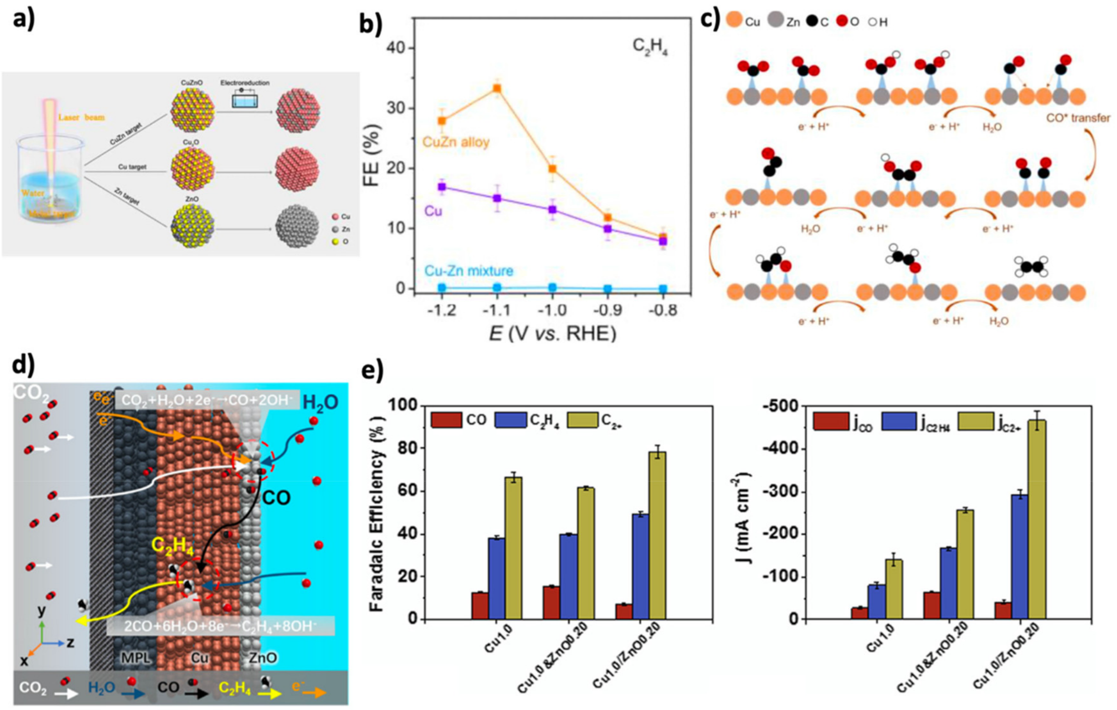

Fig. 14 (a) Schematic representation of the preparation of CuZn alloy nanoparticles, (b) faradaic efficiency of C_2H_4 obtained by eCO_2RR using CuZn alloy, Cu–Zn mixtures and Cu catalysts, (c) mechanism proposed for C_2H_4 formation with CuZn catalysts. Reprinted with permission.[201] Copyright 2018, the American Chemical Society; (d) schematic representation of use of a Cu–ZnO tandem catalyst to generate $CO_2 \rightarrow C_{2+}$, (e) faradaic efficiency and current density obtained with Cu, Cu and ZnO mixtures and Cu–ZnO tandem catalysts. Reprinted with permission.[203] Copyright 2020, Elsevier Inc.

in the catalyst leads to the emergence of phase boundaries which promote C–C coupling by increasing CO coverage and stabilising reaction intermediates. The identity and availability of the guest metal near Cu affects the concentration of CO at copper. The oxidation state of Cu in the catalyst also is significant in providing a selective pathway for ethylene or ethanol production during electrolysis. In particular, stabilisation of the Cu(I) state of the catalyst during eCO_2RR has been suggested to be crucial for the generation of highly reduced carbons,[36,196–199] but not without debate.[200]

4.3.1 Ethylene. CuZn alloy nanoparticles, prepared by Feng *et al.*,[201] have been reported to produce ethylene with considerable selectivity, as depicted in Fig. 14(a and b). In their study, the authors initially prepared CuZnO nanoparticles having different Cu : Zn ratios by the pulsed laser ablation method and electrochemically reduced them to CuZn before performing bulk electrolysis experiments. They found that CuZn nanoparticles with a 4 : 1 Cu : Zn ratio generated 33.3% ethylene at −1.15 V *vs.* RHE in 0.1 M $KHCO_3$. The reason for enhanced ethylene formation is the generation of abundant *CO associated with the presence of Zn and also the homogeneous distribution of Cu and Zn in CuZn nanoparticles that aids the transfer of *CO from Zn to Cu sites followed by CO–CO coupling over the Cu sites and then finally the release of C_2H_4 (see Fig. 14(c)).

Garcia *et al.*[202] have synthesized CuO/ZnO particles by a water/oil microemulsion method. Bulk electrolysis experiments using this catalyst in 0.1 M $KHCO_3$ using a flow cell, produced ethylene with a faradaic efficiency of 91.1% at highly negative potentials (−2.5 V *vs.* Ag/AgCl). Recently, Zhang *et al.*[203] prepared a Cu/ZnO tandem catalyst by airbrushing commercial Cu and ZnO nanoparticles over carbon paper and performed bulk electrolysis with a flow cell in 1 M KOH solution (Fig. 14(d)). With this Cu/ZnO tandem catalyst, the combination of ZnO acting as a CO generator and Cu as a C_2 intermediate stabilizer enhances C_2 and C_{2+} product formation. With an optimal loading of Cu and ZnO, Cu/ZnO tandem catalyst produces 48% ethylene at −0.7 V *vs.* RHE in 1 M KOH (Fig. 14(e)).

Use of uniformly distributed CuAg alloy nanowires prepared by electroplating in 3,5-diamino-1,2,4-triazole baths, significantly enhances C_2 product generation (ethylene in particular) during eCO_2RR in a flow reactor.[204] The faradaic efficiency of ~60% for ethylene at −0.7 V *vs.* RHE and a total current density of 300 mA cm^{-2} achieved with CuAg alloy nanowires containing 6% Ag, demonstrates superior CO_2 reduction activity as shown in Fig. 15(a). Examination of *in situ* Raman spectra shown in Fig. 15(b and c) led to the conclusion that high stability of Cu_2O layers under electrolysis conditions and the optimal availability of CO were the factors that resulted in high C_2H_4 selectivity. The

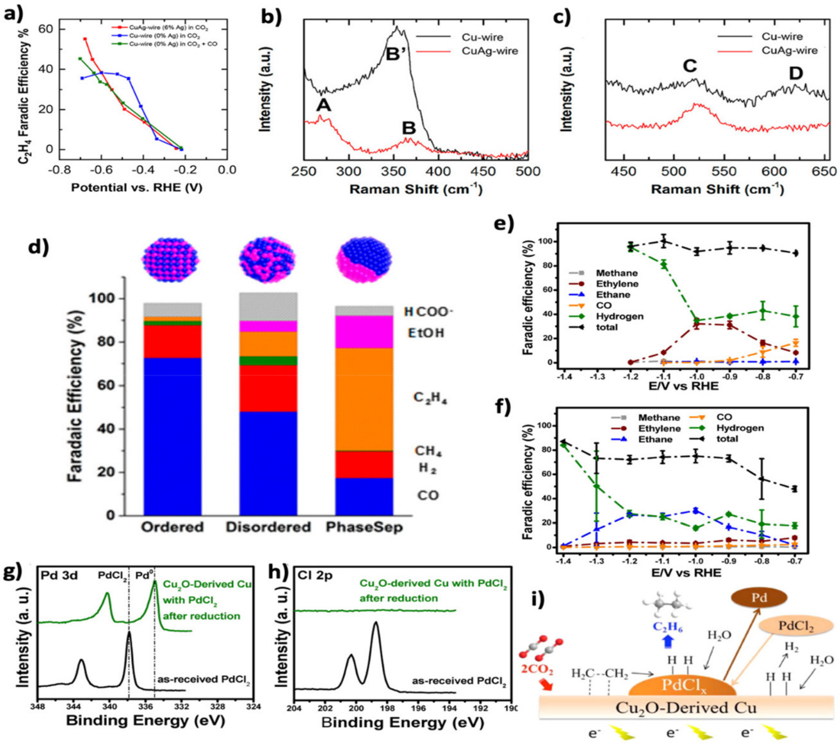

Fig. 15 (a) Faradaic efficiencies for ethylene formation obtained during electrolysis at AgCu and Cu catalysts under different experimental conditions, (b and c) *in situ* Raman spectra showing (b) the Cu–CO stretch, and (c) the Cu–O stretch regions obtained from the eCO_2RR using electrolysis AgCu and Cu catalysts at −0.7 V in 0.1 M KOH solution. Reprinted with permission.[204] Copyright 2018, American Chemical Society. (d) Faradaic efficiencies of products obtained with three CuPd catalysts. Reprinted with permission.[64] Copyright 2017, the American Chemical Society. (e and f) eCO_2RR product distribution obtained using Cu catalysts (e) with and (f) without $PdCl_2$ in the electrolyte, (g and h) XPS of (g) Pd 3d and (h) Cl 2p regions of $PdCl_2$ and a Cu catalyst with $PdCl_2$ after reduction, (i) schematic illustration of ethane formation from surface adsorbed ethylene and hydrogen using a Cu catalyst in the presence of $PdCl_2$. Reprinted with permission.[205] Copyright 2015, the American Chemical Society.

importance of the geometric arrangement in tuning the product selectivity at copper-based bimetallic catalysts is emphasized by eCO_2RR studies using alloys with different alloying configurations.[64] CuPd alloys with ordered, disordered, and phase-separated geometric structures have been examined for CO_2 reduction in 1 M KOH solution using a flow reactor. The phase-separated sample exhibited superior activity for C_2 product selectivity. A total FE for C_2 products of 63% was achieved at −0.8 V *vs.* RHE, in which the contribution from ethylene was ∼50%, as shown in Fig. 15(d). On the other hand, the selectivity for ethylene at disordered alloy sample is∼4 times lower than the phase separated sample. In contrast, the ordered CuPd alloy produced only C_1 products, mainly CO.

The significant role of $PdCl_2$ electrolyte in modifying the product selectivity achieved with Cu_2O derived Cu catalysts was identified by Yeo and co-workers.[205] With a pure Cu_2O derived Cu electrode, a 32% yield of ethylene was achieved −1.0 V *vs.* RHE in an aqueous bicarbonate solution. With addition of $PdCl_2$ into the electrolyte, a complete shift in the major product was observed with selectivity changing from C_2H_4 to C_2H_6. Now the highest faradaic efficiency was 30% for C_2H_6 at the same potential (Fig. 15(e and f)). Analysis of XPS data after electrolysis (Fig. 15(g and h)) revealed that $PdCl_2$ provides the source of a sacrificial dopant by forming Pd^0 on Cu_2O during the electrolysis reaction. According to the authors, the Pd^0 sites adsorb hydrogen effectively and provide a hydrogen source that facilitates reduction of C_2H_4 to C_2H_6, as shown in Fig. 15(i).

Tables 5 and 6 summarises the state-of-the-art Cu alloys and Cu based catalysts, which are selective for ethylene in H-type and flow cells, respectively.

4.3.2 Ethanol. The Yeo group[243] introduced oxide derived Cu_xZn catalysts for improving the selectivity for ethanol. In their study, Cu_xZn catalysts were prepared by electrodeposition of Cu_2O and ZnO layers onto a polished Cu disk from a solution containing $CuSO_4$ and $ZnCl_2$ with Cu : Zn ratios of 10, 4, 2 at a current density of −0.92 mA cm^{-2} for 600 s. Detailed characterization with selected area electron diffraction (SAED) and X-ray diffraction (XRD) techniques showed that the electrodeposited Cu_xZn consisted of phase segregated Cu and Zn crystallites rather than a CuZn alloy. eCO_2RR experiments with phase segregated Cu_xZn catalysts revealed that Cu_4Zn produced 29% ethanol at −1.05 V *vs.* RHE in 0.1 M $KHCO_3$ with a partial current density of 8.2 mA cm^{-2}. The ethanol/ethylene ratio was found to be positively correlated with the Zn content with the tested samples. On increasing the Zn content from 0% to 30% in Cu_xZn, the ethanol/ethylene ratio increased from 0.48 to 6. As shown in Fig. 16(a), it was proposed that CO generated at the Zn site spilt over to the Cu site and inserted into the $^*CH_2$ intermediate on the Cu surface, leading to the enhancement of ethanol generation.

The Grätzel group[244] reported that a CuO/ZnO core/shell structure derived CuZn bimetallic alloy catalyst for eCO_2RR achieved 41% and 48% of C_{2+} product selectivity in H-cell and flow cell configurations respectively, with ethanol being the primary C_2 product. To achieve this outcome, CuO nanowires

Table 5 Examples of state-of the art Cu alloys and other Cu based catalysts selective for ethylene generation in an H-cell by eCO_2RR

Catalyst	Electrolysis cell	Electrolyte	Potential (V *vs.* RHE)[a]	FE (%)	$j_{C_2H_4}$ (mA cm^{-2})	Ref.
OD-Cu + $PdCl_2$	H-cell	0.1 M $KHCO_3$	−1.0	32	∼10	205
$ZrO_2/Cu–Cu_2O$	H-cell	0.1 M KCl	−1.3	62.5	15	206
4H crystal phased Au/Cu nanoribbon	H-cell	0.1 M $KHCO_3$	−1.1	44.9	14.4	207
Ag/Nafion-Cu_2O	Single compartment cell	0.1 M $NaHCO_3$	−1.9	80	16	208
Ag–Cu nanodimers	Custom made two compartment cell	0.1 M $KHCO_3$	−1.1	∼40	10	209
Anodized Cu	PEEK[b]	0.1 M $KHCO_3$	−1.08	38.1	7.3	210
Plasma activated Cu	Custom made two compartment cell	0.1 M $KHCO_3$	−0.9	60	>8	211
Cu_2O derived Cu	Teflon cell[b]	0.1 M $KHCO_3$	−1.0	42.6	13.3	212
Nano-defective Cu nanosheets	H-Cell	0.1 M K_2SO_4	−1.18	83.2	∼50	213
Cu_2O film	Teflon cell[b]	0.1 M $KHCO_3$	−0.99	37.5	12.9	214
Cu mesocrystal	PTFE cell[b]	0.1 M $KHCO_3$	−0.99	27.2	7	215
B-doped Cu	H-cell	0.1 M KCl	−1.1	52	36.4	216
Plasma treated Cu	H-cell	0.1 M $KHCO_3$	−1.0	45	15.3	217
t-Cu_2O NPs/C	H-cell	0.1 M $KHCO_3$	−1.1	59	24	218
Cu_2O NPs/C	H-cell	0.1 M $KHCO_3$	−1.1	57.3	12	219
Cu_3N nanocubes	H-cell	0.1 M $KHCO_3$	−1.6	60	18	220
Pulsed-Cu	H-cell	0.1 M $KHCO_3$	−1.0	48.6	20	221
CuO_x	H-cell	0.1 M $KHCO_3$	−1.3	53	14	222
UiO-66-derived amorphous ZrO_x/Cu	H-cell	0.1 M $KHCO_3$	−1.05	43.3	15.7	223
CuBr derived Cu nanodendrites	H-cell	0.1 M $KHCO_3$	−0.85	∼40	∼9	224
Cu on Cu_3N	H-cell	0.1 M $KHCO_3$	−1.05	43	∼16.5	225
Reconstructed Cu–I	H-cell	0.1 M $KHCO_3$	−1.09	59.9	∼15.7	226
$Cu_{1.8}Se$ nanowires	H-cell	0.1 M $KHCO_3$	−1.1	55	8.3	227
A-Cu NWs	H-cell	0.1 M $KHCO_3$	−1.0	69.79	∼18	228
Cu/TiNT	H-cell	0.5 M KCl	−1.6[c]	55	132	229

[a] Potential at which maximum FE was obtained. [b] Custom made two compartment cell. [c] V *vs.* Ag/AgCl.

Table 6 Examples of state-of the art Cu alloys and other Cu based catalysts that favour ethylene formation in flow/MEA cells

Catalyst	Electrolysis cell configuration	Electrolyte	Potential (V *vs.* RHE)[a]	FE (%)	$j_{C_2H_4}$ (mA cm^{-2})	Ref.
Cu/ZnO	Plug flow reactor	1 M KOH	−0.9	~50	~300	203
CuAg nanowires	Flow cell	1 M KOH	−0.7	60	~180	204
Phase separated CuPd NPs	Flow cell	1 M KOH	−0.8	~50	~180	64
Ce doped Cu NPs	Flow cell	1 M KOH	−0.7	53	~80	230
Atomic Ni decorated Cu	Flow cell	1 M KOH	−0.88	31.8	85	231
Cu (100) nanocubes	Flow cell	1 M KOH	−0.7	60	120	191
Cu-DAT nanowires	Flow cell	1 M KOH	−0.6	38.2	90	232
Cu NPs	Flow cell	1 M KOH	−0.58	35	150	233
Graphite/carbon NPs/Cu/PTFE	Flow cell	7 M KOH	−0.55	70	~70	234
DVL-Cu	Flow cell	1 M KCl	−0.81	84.4	92.5	235
Fluorinated-Cu	Flow cell	0.75 M KOH	−0.89	65	1040	236
CuS/Cu–V	Flow cell	1 M KOH	−0.92	21.1	84	237
Dendritic Cu	Flow cell	0.1 M $KHCO_3$	−1.2	36	162	238
Nanoporous Cu	Flow cell	1 M KOH	−0.67	38.6	252	239
PTFE-Cu NPS	MEA	0.1 M $KHCO_3$	3.8b[b]	56.7	85	240
Molecular tuned Cu	MEA	1 M $KHCO_3$	3.65[b]	72	230	241
Graphite/carbonNP/Cu/PTFE	MEA	1 M $KHCO_3$	4.2[b]	46	92	242

[a] Potential at which maximum FE was obtained. [b] Cell voltage.

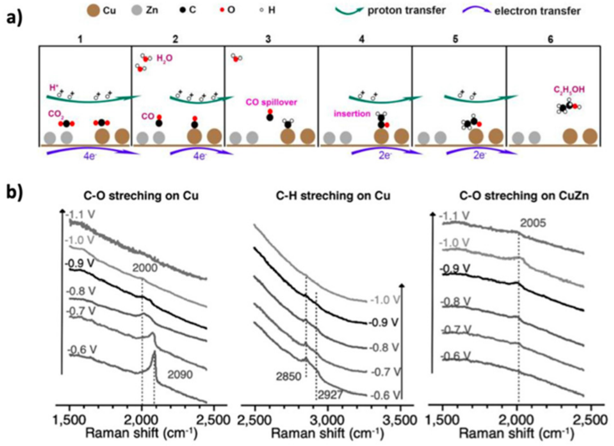

Fig. 16 (a) Mechanism proposed for ethanol formation using CuZn catalysts. Reprinted with permission.[243] Copyright 2016, the American Chemical Society. (b) Operando Raman spectra obtained during electrolysis of saturated CO_2 in 0.1 M $KHCO_3$ solution using Cu and CuZn catalysts. Reprinted with permission.[244] Copyright 2019, Wiley-VCH Verlag GmbH & Co. KGaA, Weinheim.

were coated with ZnO (~30 nm thick) by atomic layer deposition. Subsequently, electrochemical reduction was undertaken to form a CuZn bimetallic layer (~90 nm) over the Cu nanorods. XRD analysis after electroreduction showed the presence of Cu and Zn/ZnO but not CuZn alloy. This CuZn catalyst was used to catalyze eCO_2RR in 0.1 M $KHCO_3$ using an H-cell. Ethanol was produced at −1.15 V *vs.* RHE with a FE of 32% and a partial current density of 10.5 mA cm^{-2}. The mechanism proposed in this study on the basis of analysis of Raman spectra (Fig. 16(b)) is similar to that suggested by Ren *et al.*[243] for the formation of ethanol using a phase segregated Cu_xZn catalyst.

An eCO_2RR study by Lee *et al.*[63] also reveals the importance of Cu–Ag biphasic boundaries in achieving high ethanol selectivity. The structure of this catalyst allows the CO concentration near the Cu–Ag phase blended catalyst surface to be increased, facilitating the insertion of CO into the Cu bound intermediates ($*CH_2$) to form $*COCH_2$. Upon further transfer of protons and electrons, $*COCH_2$ is hydrogenated, resulting in the formation of ethanol *via* the acetaldehyde route. A recent eCO_2RR study using CuO_x coated Ag nanowires revealed an interesting relationship between the thickness of the CuO_x layer and ethanol selectivity.[245] While the Ag/CuO_x-*y* (core/shell-*y*, where *y* represents the average thickness of the shell in nm) samples with lower CuO_x thickness (Ag/CuO_x-10) showed substantial ethanol formation (Fig. 17(c)), ones with thicker CuO_x favoured ethylene. *In situ* XAS studies (Fig. 17(d)) revealed that Ag/CuO_x-10 initially contained Cu_2O which was stable in the potential range of −0.5 to −0.7 V *vs.* RHE (Cu–$O_{(Cu_2O)}$ and Cu–$Cu_{(Cu_2O)}$ bands preserved) but reduced to Cu^0 at potentials more negative than −0.7 V resulting in formation of a Cu–$Cu_{(Cu)}$ bond (Cu–Cu band of metallic Cu). However, CuAg alloy was not formed during this reduction process. With Ag/CuO_x-32, a less negative potential is sufficient to trigger this structural change. At a potential of −0.6 V *vs.* RHE, reduction of Cu_2O to metallic Cu^0 was observed. Further, in both cases this led to a stable atomic arrangement in the potential range of −0.7 to −1.3 V *vs.* RHE resulting in enhanced C_2 product selectivity. The authors found that the existence of a majority of Cu in the +1 state facilitated the CO insertion mechanism and favoured ethanol production at Ag/CuO_x-10 while the presence of more Cu^0 in Ag/CuO_x-32 favoured C–C coupling mechanism which led to the formation of ethylene. This result signifies that the transformation of Cu (I) to Cu(0) is controlled by the CuO_x thickness, which in turn influences the eCO_2RR product selectivity.

Tables 7 and 8 summarie the state-of-the-art Cu alloys and other Cu based catalysts, which are selective for ethanol in H type and flow/membrane electrode assembly (MEA) cells, respectively.

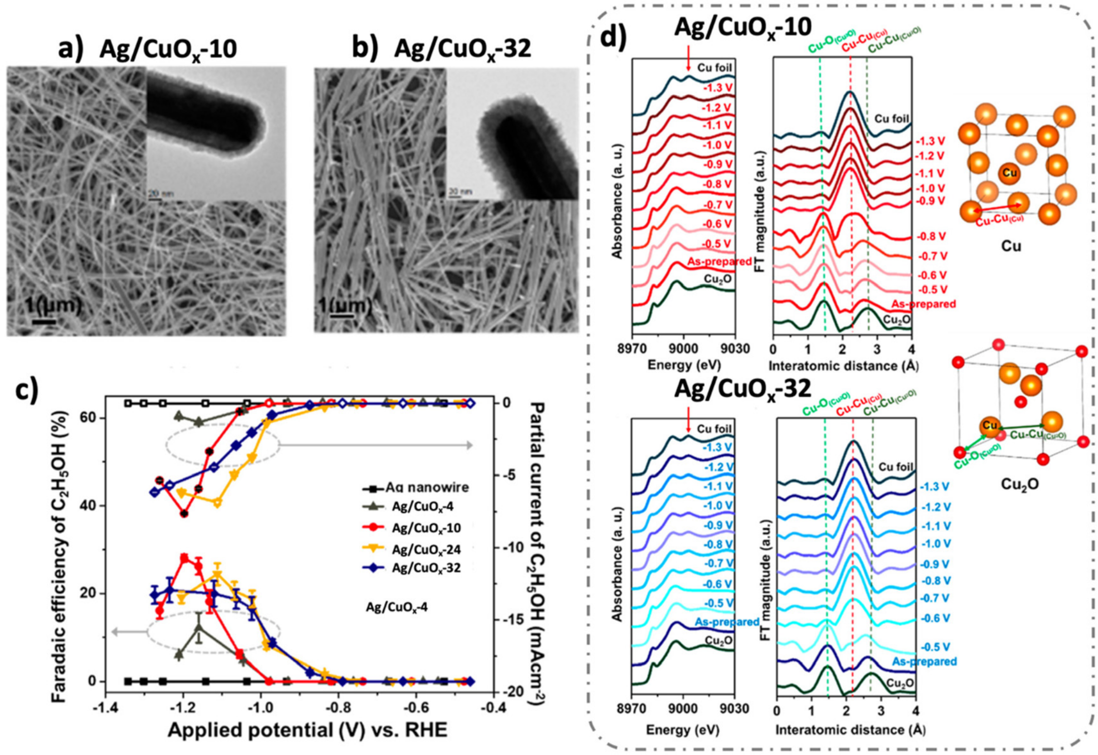

Fig. 17 (a and b) SEM images of Ag/CuO$_x$-*y* (core/shell-*y*, where *y* represents the average thickness of the shell in nm) catalysts, (c) ethanol faradaic efficiencies and partial current densities obtained with Ag/CuO$_x$-*y* catalysts, (d) *in situ* XANES and EXAFS data obtained with Ag/CuO$_x$-10 and Ag/CuO$_x$-32 catalysts. Reprinted with permission.[245] Copyright 2019, the American Chemical Society. Source: https://pubs.acs.org/doi/10.1021/acscentsci.9b01142. Further permissions related to the material excerpted should be directed to the ACS.

Table 7 Examples of state-of the art Cu alloy catalysts that favour ethanol production by eCO$_2$RR in an H-cell

Catalyst	Electrolysis cell	Electrolyte	Potential (V *vs.* RHE)[a]	FE (%)	$j_{C_2H_5OH}$ (mA cm^{-2})	Ref.
Cu_4Zn	H-cell	0.1 M $KHCO_3$	−1.05	29	8.2	243
CuO/ZnO	PEEK[b]	0.1 M $KHCO_3$	−1.15	32	10	244
Ag/CuO$_x$-10	H-cell	0.1 M $KHCO_3$	−1.2	29	7.6	245
Cu_3Sn	H-cell	0.1 M $KHCO_3$	−1.0	64	5.7	246
$Ag_{20}Cu_1$	H-cell	0.1 M $KHCO_3$	−1.1	16.5	4.1	247
Au_1Cu_3	H-cell	0.5 M $KHCO_3$	−1.0	29	5.6	248
Cu_5Zn_8	H-cell	0.1 M $KHCO_3$	−0.8	46.6	2.3	249
Dendritic Cu–Cu_2O	H-cell	0.1 M KCl	−0.4	26	2.99	250
CuO NPs	H-cell	0.2 M KI	−1.7[c]	36.1	N.R	251
Cu/carbon nanospike	H-cell	0.1 M KOH	−1.2	63	~3	252
Cu–I	H-cell	0.1 M $KHCO_3$	−0.9	25	11	253
Cu-GNC-VL	H-cell	0.5 M $KHCO_3$	−0.9	70.5	9	254
$Cu_2/N_{0.14}C$	H-cell	0.1 M $KHCO_3$	−1.1	51	14.4	255
UiO-66-derived amorphous ZrO$_x$/Cu	H-cell	0.1 M $KHCO_3$	−1.1	22.4	12.7	223
Cu on Cu_3N	H-cell	0.1 M $KHCO_3$	−0.95	18.4	~8	225
$Cu_{1.8}Se$ nanowires	H-cell	0.1 M $KHCO_3$	−1.1	24	3.5	227

N.R – not reported. [a] Potential at which maximum FE was obtained. [b] Custom made two compartment cell. [c] Potential (V) *vs.* SCE.

4.3.3 Other C_2/C_{2+} products. Apart from ethanol, acetate, propanol, and acetaldehyde are the other major oxygenates derived from CO_2 using the eCO$_2$RR with copper containing electrocatalytic materials. However, despite significant efforts to enhance the yields of these other highly reduced products, faradaic efficiencies reported to date are still very low.

Acetate formation with reasonable selectivity (faradaic efficiency of 21% at −1.3 V *vs.* RHE), at 0 °C was achieved by the Meyer group by employing ultra-small $(Cu)_m(Ag)_n$ (*m*, *n* denote the atomic ratios of Cu and Ag) bimetallic nanoparticles immobilised on a polymer. In 0.5 M $KHCO_3$ electrolyte containing 8 ppm benzotriazole at 0 °C, significant

Table 8 Examples of state-of the art Cu alloy catalysts that favour ethanol production by eCO_2RR in flow/MEA cells

Catalyst	Electrolysis cell	Electrolyte	Potential (V *vs.* RHE)[a]	FE (%)	$j_{C_2H_5OH}$ (mA cm^{-2})	Ref.
CuO/ZnO	Flow cell	1 M KOH	N.R	41	82	244
Phase separated CuPd NPs	Flow cell	1 M KOH	−0.8	~50	~180	64
Cu_9Zn_1	Flow cell	1 M KOH	−1.0	26.2	~60	256
CuAg nanowires	Flow cell	1 M KOH	−0.7	25	75	204
Binding-site diverse Ag/Cu	Flow cell	1 M KOH	−0.67	41	102	231
Ag decorated Cu/Cu_2O	Flow cell	1 M KOH	N.R	19.2	304.5	257
Atomic Ni decorated Cu	Flow cell	1 M KOH	−0.88	22.9	61.4	258
N–C/Cu	Flow cell	1 M KOH	−0.68	52	156	259
Cu_2O spheres	Flow cell	2 M KOH	−0.61	26.9	71.8	250
Cu-DAT nanowires	Flow cell	1 M KOH	−0.69	27.3	~35	232
Fluorinated-Cu	Flow cell	2.5 M KOH	−0.54	16	128	236
CuS/Cu–V	Flow cell	1 M KOH	−0.92	24.7	99	237
Nanoporous Cu	Flow cell	1 M KOH	−0.67	16.6	~108	239
$Cu\text{-}_{DS}$	Flow cell	1 M KOH	−0.95	52	52	260
Cu_2O NPs	Flow cell	2 M KOH	−0.6	~27	93	198
FeTPP[Cl]/Cu	Flow cell	1 M $KHCO_3$	−0.82	41	124	261
FeTPP[Cl]/Cu	MEA	0.1 M $KHCO_3$	3.7[b]	45	100	261
Cu_3Sn	MEA	1 M KOH	3[b]	40	361	246
PTFE-Cu NPS	MEA	0.1 M $KHCO_3$	4.2[b]	17.1	~40	240
Graphite/carbonNP/Cu/PTFE	MEA	0.1 M $KHCO_3$	4.2[b]	~15	~30	242
$Cu\text{-}_{DS}$	MEA	0.1 M $KHCO_3$	3.5[b]	50	95	260

N.R – not reported. [a] Potential at which maximum FE was obtained. [b] Cell voltage.

enhancement of acetate with a FE of 21.2% at −1.3 V *vs.* RHE was achieved on $(Cu)_m$, $(Ag)_n$ compared to pure Cu where less than 1% of acetate was produced. The CO spillover mechanism from Ag to Cu was again proposed. As for ethanol production described above, CO inserted onto the Cu surface and then coupled with $*CH_2$ to give the $*COCH_2$ intermediate, but which in this case was further reduced to acetate *via* the acetaldehyde route. Since the availability of CO at copper is the limiting factor for C–C coupling, Lum *et al.*[262] have introduced sequential Cu–Au and Cu–Ag catalysts. These were microfabricated electrodes where Cu and Au or Ag were organized in a sequential order with predefined thickness of each metal and the distance between the two metals as shown in Fig. 18(a–c). In these catalysts, Cu is in close proximity with Au or Ag and favours formation of CO during eCO_2RR. The generated CO spills over to the Cu surface and facilitates production of more highly reduced carbon fuels. By this strategy, these authors have improved the formation of oxygenate products to 41.3% which surpasses the selectivity of 26.1% achieved for hydrocarbons. The microfabricated Cu–Au or Cu–Ag electrodes used in these studies consisted of integrated but independent Cu and Au/Ag electrodes arranged adjacent to each other (Fig. 18 (a–c)). As a result, the CO generated during eCO_2RR was accumulated near adjacent Cu electrodes. By varying the distance between the Cu and Ag probes, the oxygenate to ethylene ratio can be varied from 0.5 to 2.4, with the highest faradaic efficiency of oxygenates reaching 41.4%, with total C_2/C_{2+} products being 65% (Fig. 18(d)). This study paves the way for new catalyst design strategies with controlled bimetallic arrangements for selective generation of C_2/C_{2+} products other than ethylene. Morales-Guio *et al.*[263] developed an Au/Cu tandem catalyst by depositing Au nanoparticles on Cu foil. This catalyst design provided more than a 100-fold increase in the rate of CO_2 reduction to the higher reduced carbon products. The improvement in C_2/C_{2+} alcohol production at low overpotentials was attributed to the enhanced local CO concentration provided by Au present in close proximity to copper.

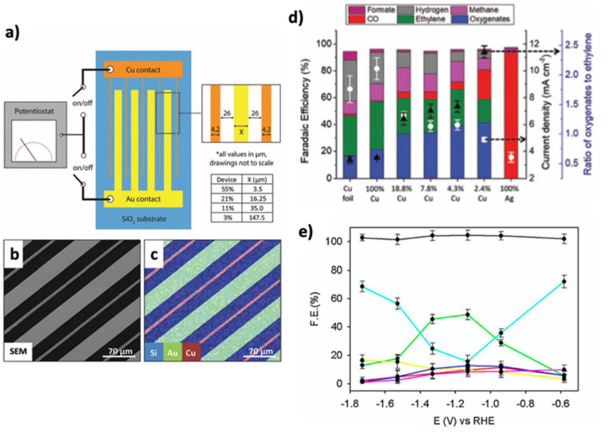

Fig. 18 (a) Schematic diagram of a custom-made electrochemical device with microfabricated Au and Cu electrodes, (b) SEM and (c) EDX mapping of AuCu electrodes with 11% of geometric area occupied by Cu, (d) faradaic efficiencies and current densities obtained with AgCu electrodes. Reprinted with permission.[262] Copyright 2018, the Royal Society of Chemistry. (e) Faradaic efficiencies of products obtained with a Mo_8/Cu heterostructure catalyst (cyan: hydrogen, red: ethanol, green: acetate, yellow: methane, blue: ethylene, purple: ethane). Reprinted with permission.[264] Copyright 2021, Elsevier B.V.

Recently, the Wu group[203] have reported that enhancement in oxygenate production also can be achieved with a Cu/ZnO tandem catalyst. Tandem catalysts with variable ZnO loading were prepared by air brushing ZnO onto a Cu electrode presynthesised on a GDL electrode and dried under vacuum. By

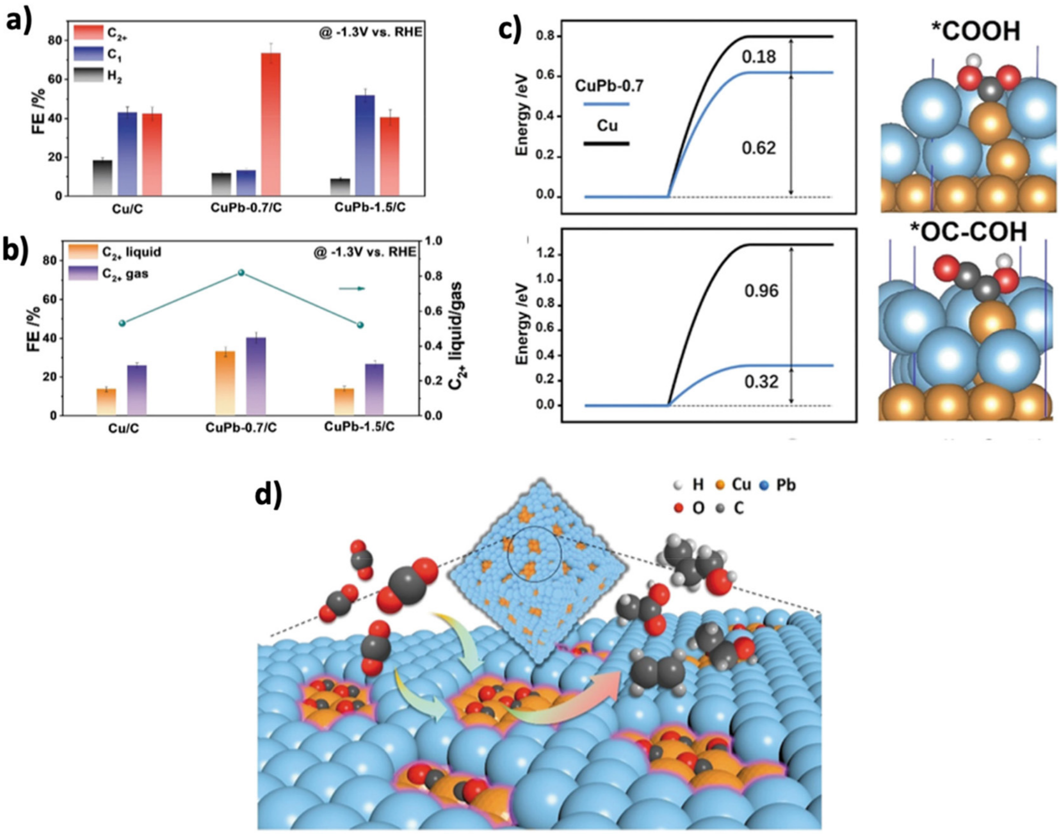

Fig. 19 (a and b) Faradaic efficiencies of C_1 and C_2 products obtained using a CuPb-0.7/C (where 0.7 represents the thickness of Pb shell) catalyst, (c) simulated data and (d) schematic illustration of the production of C_{2+} products *via* the eCO$_2$RR route. Reprinted with permission.[265] Copyright 2021, the American Chemical Society.

controlling the ZnO loading, effective spatial management of CO transport was achieved to optimise CO utilisation. High selectivity for C_{2+} products with a faradaic efficiency reaching 80% is achieved as shown in Fig. 14(e) with a partial current density of ~470 mA cm^{-2} obtained with $Cu_{1.0}Zn_{0.2}$, values which respectively are 1.2 and 3.4 times higher than obtained with pure Cu.

An excellent conversion yield for CO_2 to acetate was reported recently at polyoxometalate modified Cu cubes. The Mo_8/Cu heterostructure catalyst was rich in Cu–O–Mo interfaces, which led to the generation of acetate with a FE of 48.8% at −1.13 V (Fig. 18(e)) and a partial current density of 68.9 mA cm^{-2} in saturated $NaHCO_3$.[264] The selectivity for C_{2+} products was found to be dependent on the thickness of the shell in Cu/Pb core/shell nanocubes. Cu/Pb nanocubes with an optimal shell thickness of 0.7 nm gave 73.5% C_{2+} products with a partial current density of 294.4 mA cm^{-2} at −1.3 V in 1 M KOH solution under flow cell conditions (Fig. 19(a and b)).[265] DFT calculations

Table 9 Examples of the state-of-the-art Cu alloys and other Cu based catalysts for other C_2/C_{2+} product formation with eCO$_2$RR

Catalyst	Product	Electrolysis cell	Electrolyte	Potential (V *vs.* RHE)[a]	FE (%)	$j_{product}$ (mA cm^{-2})	Ref.
$(Cu)_m$, $(Ag)_n$ NPs	CH_3COO^-	H-cell	0.5 M $KHCO_3$ + 8 ppm benzotriazole	−1.33	21	N.R	267
Dendritic Cu–Cu_2O	CH_3COO^-	H-cell	0.1 M KCl	−0.4	40	4.6	250
4% Cu dots/Ag	Oxygenates	PEEK[b]	0.1 M $CsHCO_3$	−1.0	41	4.4	262
Mo_8/Cu	CH_3COO^-	Electrochemical batch cell	Saturated $NaHCO_3$	−1.13	49	57	264
CuBi	C_3H_8	Filter press cell	0.45 M $KHCO_3$ + 0.5 M KCl.	N.R	85	38	266
Single atom Cu/NPC	CH_3COCH_3	H-cell	0.1 M $KHCO_3$	−0.36	36.7	N.R	268
CuI derived Cu nanofibres	C_2H_6	H-cell	0.1 M $KHCO_3$	−0.73	~30	~9	224
CuS_x-DSV	n-C_3H_7OH	H-cell	0.1 M $KHCO_3$	−1.05	15.4	~10	269
Graphene/ZnO/Cu_2O	n-C_3H_7OH	H-cell	0.5 M $NaHCO_3$	−0.9[c]	30	N.R	270
MOF derived Cu	n-C_3H_7OH	Five port electrochemical cell	0.1 M $KHCO_3$	−2.4[c]	~16	~4	271

N.R – not reported. [a] Potential at which maximum FE was obtained. [b] Custom made two compartment cell. [c] V *vs.* Ag/AgCl.

revealed that the synergistic effects due to the core/shell structure decreased the formation energies of *COOH and *OCCOH intermediates, thereby facilitating production of highly reduced carbon products as shown in Fig. 19(c and d). Azenha *et al.*[266] reported the production of propane with a remarkable FE of 84.6% by employing Bi coated CuO nanowires on a filter press cell in 1 M KOH. Bidentate carbonate formation on the catalyst surface was an important requirement for the formation of propane. Detailed investigations revealed that the presence of Cu(I) sites and oxygen defects influenced the binding affinity of CO_2 to the Bi/Cu NW catalyst in a manner which led to high selectivity for propane.

Table 9 summarises the state-of-the-art Cu alloys and other Cu based catalysts, which are selective for other C_2/C_{2+} products.

5. Conclusions and future directions

The development of rationally designed Cu based alloy catalysts is helping to address the problem of low product selectivity achieved by eCO_2RR with pristine Cu. The reaction pathways can be manipulated by geometric and electronic effects that arise upon alloying a material. The choice of the guest elements alloyed with Cu and the spatial distribution of the constituent elements are crucial in determining the selectivity of eCO_2RR products. In this review, the different strategies reported for alloying and their influence on the properties of the catalyst are surveyed. Achievements based on state-of-the-art Cu based alloy catalysts that improve the selectivity of the targeted product are highlighted.

Commonly, the selectivity of the product is related to the binding energies of key reaction intermediates which can be tuned by varying the structure of the alloy. For example, in alloys with ordered atomic structures, the elemental composition influences the bond length between the elements. This, in turn, influences the binding energies of eCO_2RR intermediates adsorbed onto the catalyst surface, providing a systematic route to tuning product selectivity. On the other hand, a disordered alloy system can lead to changes in electronic and geometric structures during electrolysis which also influences the products that are formed. In the case of a core/shell type alloy structure, it is the strain and ligand effects, atomic vacancies and doping that affect the binding strength of reaction intermediates, again providing systematic routes to selectively tuning the product formation pathway. Phase separated alloys enhance the product selectivity in a unique way. In this class of alloy there is a clear separation in the phases of the different elements in the alloy, allowing each phase to individually generate the product that is characteristic of the element in the particular phase. Migration of products or the coupling of intermediates at the boundary of different phases is possible. This helps in producing highly reduced carbon products such as ethylene or ethanol with enhanced selectivity generally facilitated by the CO spillover mechanism.

Strategic alloying can introduce specific synergistic effects that are useful to tune the selectivity towards each product. However, other inevitably coupled effects could diminish the product selectivity. Hence, despite the ability to manipulate the reaction pathways by altering the binding energies, complete selectivity for one product remains exceedingly difficult to achieve when an alloying strategy is used alone. Therefore, integration with other catalyst design strategies is highly recommended.

Alloy structures also tend to be unstable under electrolysis conditions. The lifetime for most of the catalysts used to date is typically within a day, which is far less than that required for commercial applications. To address the problem of stability, high entropy alloys are now receiving considerable attention. These are a new class of alloy formed with multiple elements. HEAs are highly stable under extreme conditions, such as high temperatures and prolonged electrolysis conditions due to an exceptionally high kinetic solid diffusion barrier. They are active for eCO_2RR, and in principle the electronic properties and hence selectivity can be precisely tuned as they possess exceptional flexibility for adjusting the binding energy compared to primitive alloys. HEAs consist of a minimum of five different elements, resulting in a wide range of compositions and atomic arrangements. Hence, powerful machine learning tools[272,273] are needed to identify the optimal composition and structure required to achieve selective generation of a desired eCO_2RR product. Even though the suitable composition and structure of the HEAs are predicted theoretically, the currently used synthesis strategies for HEAs require high temperatures, pressures and an inert environment. Precisely controlling the microstructures or the local atomic arrangement also is highly complicated.[274,275]

The synergistic, so called "cocktail effect" displayed by HEAs with their multiple elemental combinations exhibit exceptional binding energies for reaction intermediates. The availability of different binding sites in these catalysts also can provide the possibility of wide range of binding energies for eCO_2RR intermediates and thus provide the possibility to tune the selectivity of the products.[274] This property can be advantageous for cascade reactions, where the product formed at one binding site is desorbed from the surface and re-bound at the other for further reaction. Hence the choice of elements and atomic arrangement in the catalyst should be given priority when designing these catalysts. Copper based high entropy alloys are a focus as they provide the possibility of producing highly reduced hydrocarbon fuels with improved selectivity by means of cascade reactions. Support from theoretical studies is critical to extricate the full potential of such alloys.[66,72,276] Despite these highly attractive properties, application of HEAs in the eCO_2RR is still limited.[274,275] Nellaiappan *et al.*[277] achieved the first experimental realization of the application of nanocrystalline HEAs for eCO_2RR. Nanocrystalline AuAgPtPdCu produces 100% of gaseous products including CO, CH_4 and C_2H_4 at a low potential of −0.3 V *vs.* RHE with high hydrocarbon (CH_4 + C_2H_4) selectivity (~70%) in aqueous 0.5 M K_2SO_4. First principle based DFT calculations attribute this outcome to the destabilisation of

*OCH_3 and highly enhanced stabilisation of *O intermediates. Pedersen *et al.*[66] investigated the possibility of the formation of multicarbon products at HEAs by combining DFT with machine learning with (111) facets of CoCuGaNiZn and AgAuCuPdPt as model systems. The authors established a correlation between composition and the variation in H and CO binding energies.

In addition to achieving a more rational design of catalyst material, understanding the mechanism of eCO_2RR at the atomic level should make it possible to establish more precise structure–property relationships. From this perspective, advanced *in situ* characterisation techniques are receiving increased attention.[278–280] Several studies have shown that mixed oxidation states of Cu stabilise reaction intermediates that produce highly reduced C_2 fuels.[43,65,198,210,281] However, recent *in situ* studies through a combination of synchrotron based grazing incidence X-ray absorption and X-ray diffraction spectroscopy have suggested that Cu is present in the metallic 0 oxidation state during electrolysis.[200] Such contradictory results may be due to structural differences in the catalytic materials. Clearly, morphological and structural changes in the catalyst during electrolysis need to be monitored. Development of more sensitive *in situ* spectroscopic and microscopic structural characterisation tools is needed.

Finally, the electrolysis system design must be optimised to enhance mass transport rates for both reactants and products. Recent research has demonstrated that use of gas diffusion electrodes and membrane electrode assemblies allow current densities to be increased drastically compared to those achievable with conventional H-shaped electrolysis cells.[234,282,283] Improved cell designs and reaction conditions that allow much higher current densities, lower resistance and higher stability are essential to reach commercially viable efficiencies. So far, high purity CO_2 gas has been commonly used in eCO_2RR studies. To fully realize the potential of the eCO_2RR for commercial application, the effect of impurities, such as SO_x, NO_x, which are commonly present in the industrial flue gases, should be investigated. However, research towards this direction is still limited.[284]

In summary, eCO_2RR is a viable method for utilising CO_2. However, even though eCO_2RR can produce a variety of commercially valuable fuels, manufacturing of targeted products with high selectivity remains difficult. Using catalysts derived from alloying with Cu addresses some of the limitations since it allows considerable control over product selectivity by changing the guest element and the alloy structure. Despite many significant achievements emerging from the development of efficient Cu based alloy catalysts, fabrication of catalysts that have high stability and can generate significantly reduced carbon products in commercially viable quantities at competitive prices remains highly challenging.

Conflicts of interest

There are no conflicts to declare.

Acknowledgements

The authors thank the Australian Research Council for financial support though the ARC Centre of Excellence for Electromaterials Science.

References

1 R. B. Jackson, C. Le Quéré, R. M. Andrew, J. G. Canadell, G. P. Peters, J. Roy and L. Wu, *Environ. Res. Lett.*, 2017, **12**, 110202.

2 Carbon dioxide peaks near 420 parts per million at Mauna Loa observatory, **https://research.noaa.gov/article/ArtMID/587/ArticleID/2742/Despite-pandemic-shutdowns-carbon-dioxide-and-methane-surged-in-2020**, **https://research.noaa.gov/article/ArtMID/587/ArticleID/2764/Coronavirus-response-barely-slows-rising-carbon-dioxide**, (accessed 10.05.2022, **https://research.noaa.gov/article/ArtMID/587/ArticleID/2764/Coronavirus-response-barely-slows-rising-carbon-dioxide**).

3 I. Sullivan, A. Goryachev, I. A. Digdaya, X. Li, H. A. Atwater, D. A. Vermaas and C. Xiang, *Nat. Catal.*, 2021, **4**, 952–958.

4 J. Albero, Y. Peng and H. García, *ACS Catal.*, 2020, **10**, 5734–5749.

5 A. Hezam, K. Namratha, Q. A. Drmosh, D. Ponnamma, J. Wang, S. Prasad, M. Ahamed, C. Cheng and K. Byrappa, *ACS Appl. Nano Mater.*, 2020, **3**, 138–148.

6 Z. Hu and W. Liu, *ACS Appl. Mater. Interfaces*, 2020, **12**, 51366–51373.

7 J. Ran, M. Jaroniec and S.-Z. Qiao, *Adv. Mater.*, 2018, **30**, 1704649.

8 F. L. Sousa, M. Preiner and W. F. Martin, *Curr. Opin. Microbiol.*, 2018, **43**, 77–83.

9 A. M. Appel, J. E. Bercaw, A. B. Bocarsly, H. Dobbek, D. L. DuBois, M. Dupuis, J. G. Ferry, E. Fujita, R. Hille, P. J. A. Kenis, C. A. Kerfeld, R. H. Morris, C. H. F. Peden, A. R. Portis, S. W. Ragsdale, T. B. Rauchfuss, J. N. H. Reek, L. C. Seefeldt, R. K. Thauer and G. L. Waldrop, *Chem. Rev.*, 2013, **113**, 6621–6658.

10 D. Dong, P. Aleta, X. Zhao, O. K. Choi, S. Kim and J. W. Lee, *Bioresour. Technol.*, 2019, **275**, 314–320.

11 S. Roy, A. Cherevotan and S. C. Peter, *ACS Energy Lett.*, 2018, **3**, 1938–1966.

12 E. Sediva, A. J. Carrillo, C. E. Halloran and J. L. M. Rupp, *ACS Appl. Energy Mater.*, 2021, **4**, 1474–1483.

13 R. R. Bhosale, G. Takalkar, P. Sutar, A. Kumar, F. AlMomani and M. Khraisheh, *Int. J. Hydrogen Energy*, 2019, **44**, 34–60.

14 X. Chang, T. Wang and J. Gong, *Energy Environ. Sci.*, 2016, **9**, 2177–2196.

15 S. Roy and S. C. Peter, in *Advances in the Chemistry and Physics of Materials*, 2019, pp. 399–428, DOI: **10.1142/9789811211331_0017**.

16 P. R. Yaashikaa, P. S. Kumar, S. J. Varjani and A. Saravanan, *J. CO2 Util.*, 2019, **33**, 131–147.

17 S. Nitopi, E. Bertheussen, S. B. Scott, X. Liu, A. K. Engstfeld, S. Horch, B. Seger, I. E. L. Stephens, K. Chan, C. Hahn, J. K. Nørskov, T. F. Jaramillo and I. Chorkendorff, *Chem. Rev.*, 2019, **119**, 7610–7672.

18 J. Resasco, L. D. Chen, E. Clark, C. Tsai, C. Hahn, T. F. Jaramillo, K. Chan and A. T. Bell, *J. Am. Chem. Soc.*, 2017, **139**, 11277–11287.

19 Y. Lum, B. Yue, P. Lobaccaro, A. T. Bell and J. W. Ager, *J. Phys. Chem. C*, 2017, **121**, 14191–14203.

20 J. Resasco, Y. Lum, E. Clark, J. Z. Zeledon and A. T. Bell, *ChemElectroChem*, 2018, **5**, 1064–1072.

21 J. E. Pander III, D. Ren, Y. Huang, N. W. X. Loo, S. H. L. Hong and B. S. Yeo, *ChemElectroChem*, 2018, **5**, 219–237.

22 M. König, J. Vaes, E. Klemm and D. Pant, *iScience*, 2019, **19**, 135–160.

23 A. Wagner, C. D. Sahm and E. Reisner, *Nat. Catal.*, 2020, **3**, 775–786.

24 E. R. Corson, E. B. Creel, R. Kostecki, J. J. Urban and B. D. McCloskey, *Electrochim. Acta*, 2021, **374**, 137820.

25 A. Vasileff, C. Xu, Y. Jiao, Y. Zheng and S.-Z. Qiao, *Chem*, 2018, **4**, 1809–1831.

26 F. Li, L. Chen, G. P. Knowles, D. R. MacFarlane and J. Zhang, *Angew. Chem., Int. Ed.*, 2017, **56**, 505–509.

27 T. Burdyny and W. A. Smith, *Energy Environ. Sci.*, 2019, **12**, 1442–1453.

28 C.-T. Dinh, T. Burdyny, M. G. Kibria, A. Seifitokaldani, C. M. Gabardo, F. P. García de Arquer, A. Kiani, J. P. Edwards, P. De Luna, O. S. Bushuyev, C. Zou, R. Quintero-Bermudez, Y. Pang, D. Sinton and E. H. Sargent, *Science*, 2018, **360**, 783–787.

29 C.-T. Dinh, F. P. García de Arquer, D. Sinton and E. H. Sargent, *ACS Energy Lett.*, 2018, **3**, 2835–2840.

30 D. M. Weekes, D. A. Salvatore, A. Reyes, A. Huang and C. P. Berlinguette, *Acc. Chem. Res.*, 2018, **51**, 910.

31 D. Higgins, C. Hahn, C. Xiang, T. F. Jaramillo and A. Z. Weber, *ACS Energy Lett.*, 2019, **4**, 317.

32 K. Liu, W. A. Smith and T. Burdyny, *ACS Energy Lett.*, 2019, **4**, 639–643.

33 C. Delacourt, P. L. Ridgway, J. B. Kerr and J. Newman, *J. Electrochem. Soc.*, 2008, **155**, B42.

34 L. M. Aeshala, R. Uppaluri and A. Verma, *Phys. Chem. Chem. Phys.*, 2014, **16**, 17588–17594.

35 N. Gutiérrez-Guerra, L. Moreno-López, J. C. Serrano-Ruiz, J. L. Valverde and A. de Lucas-Consuegra, *Appl. Catal., B*, 2016, **188**, 272–282.

36 C. Xiao and J. Zhang, *ACS Nano*, 2021, **15**, 7975–8000.

37 M. B. Ross, P. De Luna, Y. Li, C.-T. Dinh, D. Kim, P. Yang and E. H. Sargent, *Nat. Catal.*, 2019, **2**, 648–658.

38 K. P. Kuhl, E. R. Cave, D. N. Abram and T. F. Jaramillo, *Energy Environ. Sci.*, 2012, **5**, 7050–7059.

39 A. S. Varela, W. Ju, T. Reier and P. Strasser, *ACS Catal.*, 2016, **6**, 2136–2144.

40 A. A. Peterson, F. Abild-Pedersen, F. Studt, J. Rossmeisl and J. K. Nørskov, *Energy Environ. Sci.*, 2010, **3**, 1311–1315.

41 Y. Hori, I. Takahashi, O. Koga and N. Hoshi, *J. Phys. Chem. B*, 2002, **106**, 15–17.

42 B. Zhang, B. Zhang, Y. Jiang, T. Ma, H. Pan and W. Sun, *Small*, 2021, **17**, 2101443.

43 G. M. Tomboc, S. Choi, T. Kwon, Y. J. Hwang and K. Lee, *Adv. Mater.*, 2020, **32**, 1908398.

44 A. R. Woldu, Z. Huang, P. Zhao, L. Hu and D. Astruc, *Coord. Chem. Rev.*, 2022, **454**, 214340.

45 C. E. Creissen and M. Fontecave, *Nat. Commun.*, 2022, **13**, 2280.

46 C. Cao and Z. Wen, *J. CO2 Util.*, 2017, **22**, 231–237.

47 P. Huang, S. Ci, G. Wang, J. Jia, J. Xu and Z. Wen, *J. CO2 Util.*, 2017, **20**, 27–33.

48 P. Shao, S. Ci, L. Yi, P. Cai, P. Huang, C. Cao and Z. Wen, *ChemElectroChem*, 2017, **4**, 2593–2598.

49 J. Jia, X. Hao, Y. Chang, M. Jia and Z. Wen, *J. Colloid Interface Sci.*, 2021, **586**, 491–497.

50 J. He, N. J. J. Johnson, A. Huang and C. P. Berlinguette, *ChemSusChem*, 2018, **11**, 48–57.

51 C. Kim, F. Dionigi, V. Beermann, X. Wang, T. Möller and P. Strasser, *Adv. Mater.*, 2019, **31**, 1805617.

52 Y. Jia, F. Li, K. Fan and L. Sun, *Adv. Powder Technol.*, 2022, **1**, 100012.

53 G. Wang, J. Chen, Y. Ding, P. Cai, L. Yi, Y. Li, C. Tu, Y. Hou, Z. Wen and L. Dai, *Chem. Soc. Rev.*, 2021, **50**, 4993–5061.

54 P. Devi, R. Verma and J. P. Singh, *J. CO2 Util.*, 2022, **65**, 102211.

55 M. Watanabe, M. Shibata, A. Kato, M. Azuma and T. Sakata, *J. Electrochem. Soc.*, 1991, **138**, 3382–3389.

56 V. Ponec, *Appl. Catal., A*, 2001, **222**, 31–45.

57 L. Xie, J. Liang, C. Priest, T. Wang, D. Ding, G. Wu and Q. Li, *Chem. Commun.*, 2021, **57**, 1839–1854.

58 H. Y. Kim and S. H. Joo, *J. Mater. Chem. A*, 2020, **8**, 8195–8217.

59 A. Groß, *Top. Catal.*, 2006, **37**, 29–39.

60 A. Schlapka, M. Lischka, A. Groß, U. Käsberger and P. Jakob, *Phys. Rev. Lett.*, 2003, **91**, 016101.

61 Y. Gauthier, M. Schmid, S. Padovani, E. Lundgren, V. Buš, G. Kresse, J. Redinger and P. Varga, *Phys. Rev. Lett.*, 2001, **87**, 036103.

62 K. Sun, T. Cheng, L. Wu, Y. Hu, J. Zhou, A. Maclennan, Z. Jiang, Y. Gao, W. A. Goddard and Z. Wang, *J. Am. Chem. Soc.*, 2017, **139**, 15608–15611.

63 S. Lee, G. Park and J. Lee, *ACS Catal.*, 2017, **7**, 8594–8604.

64 S. Ma, M. Sadakiyo, M. Heima, R. Luo, R. T. Haasch, J. I. Gold, M. Yamauchi and P. J. A. Kenis, *J. Am. Chem. Soc.*, 2017, **139**, 47–50.

65 V. S. S. Mosali, X. Zhang, Y. Liang, L. Li, G. Puxty, M. D. Horne, A. Brajter-Toth, A. M. Bond and J. Zhang, *ChemSusChem*, 2021, **14**, 2924–2934.

66 J. K. Pedersen, T. A. A. Batchelor, A. Bagger and J. Rossmeisl, *ACS Catal.*, 2020, **10**, 2169–2176.

67 X. Wang, W. Guo and Y. Fu, *J. Mater. Chem. A*, 2021, **9**, 663–701.

68 Y. Zhang, D. Wang and S. Wang, *Small*, 2022, **18**, 2104339.

69 K. Y. Tsai, M. H. Tsai and J. W. Yeh, *Acta Mater.*, 2013, **61**, 4887–4897.

70 Y. Zhang, T. T. Zuo, Z. Tang, M. C. Gao, K. A. Dahmen, P. K. Liaw and Z. P. Lu, *Prog. Mater. Sci.*, 2014, **61**, 1–93.

71 S. Chen, H. S. Oh, B. Gludovatz, S. J. Kim, E. S. Park, Z. Zhang, R. O. Ritchie and Q. Yu, *Nat. Commun.*, 2020, **11**, 826.

72 T. Löffler, A. Ludwig, J. Rossmeisl and W. Schuhmann, *Angew. Chem., Int. Ed.*, 2021, **60**, 26894–26903.

73 W. Zhang, C. Xu, Y. Hu, S. Yang, L. Ma, L. Wang, P. Zhao, C. Wang, J. Ma and Z. Jin, *Nano Energy*, 2020, **73**, 104796.

74 Y.-X. Duan, K.-H. Liu, Q. Zhang, J.-M. Yan and Q. Jiang, *Small Methods*, 2020, **4**, 1900846.

75 W. Zhang, Y. Hu, L. Ma, G. Zhu, P. Zhao, X. Xue, R. Chen, S. Yang, J. Ma, J. Liu and Z. Jin, *Nano Energy*, 2018, **53**, 808–816.

76 M. Zhao, Y. Gu, W. Gao, P. Cui, H. Tang, X. Wei, H. Zhu, G. Li, S. Yan, X. Zhang and Z. Zou, *Appl. Catal., B*, 2020, **266**, 118625.

77 P. Su, W. Xu, Y. Qiu, T. Zhang, X. Li and H. Zhang, *ChemSusChem*, 2018, **11**, 848–853.

78 W. Zhang, S. Yang, M. Jiang, Y. Hu, C. Hu, X. Zhang and Z. Jin, *Nano Lett.*, 2021, **21**, 2650–2657.

79 J. Huang, X. Guo, Y. Wei, Q. Hu, X. Yu and L. Wang, *J. CO2 Util.*, 2019, **33**, 166–170.

80 Y. Chen and M. W. Kanan, *J. Am. Chem. Soc.*, 2012, **134**, 1986–1989.

81 F. Cheng, X. Zhang, K. Mu, X. Ma, M. Jiao, Z. Wang, P. Limpachanangkul, B. Chalermsinsuwan, Y. Gao, Y. Li, Z. Chen and L. Liu, *Energy Technol.*, 2021, **9**, 2000799.

82 F. Li, L. Chen, M. Xue, T. Williams, Y. Zhang, D. R. MacFarlane and J. Zhang, *Nano Energy*, 2017, **31**, 270–277.

83 J. Gu, F. Héroguel, J. Luterbacher and X. Hu, *Angew. Chem., Int. Ed.*, 2018, **57**, 2943–2947.

84 J. Huang, X. Guo, X. Huang and L. Wang, *Electrochim. Acta*, 2019, **325**, 134923.

85 X. Huang, J. Song, H. Wu, C. Xie, M. Hua, Y. Hu and B. Han, *ChemSusChem*, 2020, **13**, 6346–6352.

86 S. Back, J.-H. Kim, Y.-T. Kim and Y. Jung, *Phys. Chem. Chem. Phys.*, 2016, **18**, 9652–9657.

87 Y. Wang, J. Liu, Y. Wang, A. M. Al-Enizi and G. Zheng, *Small*, 2017, **13**, 1701809.

88 V. S. K. Yadav and M. K. Purkait, *RSC Adv.*, 2015, **5**, 40414–40421.

89 D. Gao, H. Zhou, F. Cai, J. Wang, G. Wang and X. Bao, *ACS Catal.*, 2018, **8**, 1510–1519.

90 B. Jiang, X.-G. Zhang, K. Jiang, D.-Y. Wu and W.-B. Cai, *J. Am. Chem. Soc.*, 2018, **140**, 2880–2889.

91 F. Cai, D. Gao, H. Zhou, G. Wang, T. He, H. Gong, S. Miao, F. Yang, J. Wang and X. Bao, *Chem. Sci.*, 2017, **8**, 2569–2573.

92 T.-W. Jiang, Y.-W. Zhou, X.-Y. Ma, X. Qin, H. Li, C. Ding, B. Jiang, K. Jiang and W.-B. Cai, *ACS Catal.*, 2021, **11**, 840–848.

93 F. Zhou, H. Li, M. Fournier and D. R. MacFarlane, *ChemSusChem*, 2017, **10**, 1509–1516.

94 P. Huang, M. Cheng, H. Zhang, M. Zuo, C. Xiao and Y. Xie, *Nano Energy*, 2019, **61**, 428–434.

95 F. Li, M. Xue, J. Li, X. Ma, L. Chen, X. Zhang, D. R. MacFarlane and J. Zhang, *Angew. Chem., Int. Ed.*, 2017, **56**, 14718–14722.

96 Z. Jiang, T. Wang, J. Pei, H. Shang, D. Zhou, H. Li, J. Dong, Y. Wang, R. Cao, Z. Zhuang, W. Chen, D. Wang, J. Zhang and Y. Li, *Energy Environ. Sci.*, 2020, **13**, 2856–2863.

97 N. Han, P. Ding, L. He, Y. Li and Y. Li, *Adv. Energy Mater.*, 2020, **10**, 1902338.

98 Q. Li, X. Zhang, X. Zhou, Q. Li, H. Wang, J. Yi, Y. Liu and J. Zhang, *J. CO2 Util.*, 2020, **37**, 106–112.

99 V. S. S. Mosali, X. Zhang, Y. Zhang, T. Gengenbach, S.-X. Guo, G. Puxty, M. D. Horne, A. M. Bond and J. Zhang, *ACS Sustainable Chem. Eng.*, 2019, **7**, 19453–19462.

100 K. Ohkawa, Y. Noguchi, S. Nakayama, K. Hashimoto and A. Fujishima, *J. Electroanal. Chem.*, 1993, **348**, 459–464.

101 K. Ohkawa, Y. Noguchi, S. Nakayama, K. Hashimoto and A. Fujishima, *J. Electroanal. Chem.*, 1994, **367**, 165–173.

102 X. Zhang, F. Li, Y. Zhang, A. M. Bond and J. Zhang, *J. Mater. Chem. A*, 2018, **6**, 7851–7858.

103 W. He, I. Liberman, I. Rozenberg, R. Ifraemov and I. Hod, *Angew. Chem., Int. Ed.*, 2020, **59**, 8262–8269.

104 Y. Hori, in *Modern Aspects of Electrochemistry*, ed. C. Vayenas, Springer, New York, 2008, vol. 42, ch. 3, p. 89.

105 M. Zhao, H. Tang, Q. Yang, Y. Gu, H. Zhu, S. Yan and Z. Zou, *ACS Appl. Mater. Interfaces*, 2020, **12**, 4565–4571.

106 M. Morimoto, Y. Takatsuji, K. Hirata, T. Fukuma, T. Ohno, T. Sakakura and T. Haruyama, *Electrochim. Acta*, 2018, **290**, 255–261.

107 J. Rosen, G. S. Hutchings, Q. Lu, R. V. Forest, A. Moore and F. Jiao, *ACS Catal.*, 2015, **5**, 4586–4591.

108 T. Zhang, X. Li, Y. Qiu, P. Su, W. Xu, H. Zhong and H. Zhang, *J. Catal.*, 2018, **357**, 154–162.

109 W. Luo, J. Zhang, M. Li and A. Züttel, *ACS Catal.*, 2019, **9**, 3783–3791.

110 D. Sun, X. Xu, Y. Qin, S. P. Jiang and Z. Shao, *ChemSusChem*, 2020, **13**, 39–58.

111 M. Ma, K. Liu, J. Shen, R. Kas and W. A. Smith, *ACS Energy Lett.*, 2018, **3**, 1301–1306.

112 S. Y. Chae, S. Y. Lee and O.-S. Joo, *Electrochim. Acta*, 2019, **303**, 118–124.

113 S. A. Mahyoub, F. A. Qaraah, C. Chen, F. Zhang, S. Yan and Z. Cheng, *Sustainable Energy Fuels*, 2020, **4**, 50–67.

114 X. Peng, S. G. Karakalos and W. E. Mustain, *ACS Appl. Mater. Interfaces*, 2018, **10**, 1734–1742.

115 S. Chen and A. Chen, *J. Phys. Chem. C*, 2019, **123**, 23898–23906.

116 Y. Fang and J. C. Flake, *J. Am. Chem. Soc.*, 2017, **139**, 3399–3405.

117 H.-E. Lee, K. D. Yang, S. M. Yoon, H.-Y. Ahn, Y. Y. Lee, H. Chang, D. H. Jeong, Y.-S. Lee, M. Y. Kim and K. T. Nam, *ACS Nano*, 2015, **9**, 8384–8393.

118 J. A. Trindell, J. Clausmeyer and R. M. Crooks, *J. Am. Chem. Soc.*, 2017, **139**, 16161–16167.

119 S. Mezzavilla, S. Horch, I. E. L. Stephens, B. Seger and I. Chorkendorff, *Angew. Chem., Int. Ed.*, 2019, **58**, 3774–3778.

120 Y. Zhao, X. Tan, W. Yang, C. Jia, X. Chen, W. Ren, S. C. Smith and C. Zhao, *Angew. Chem., Int. Ed.*, 2020, **59**, 21493–21498.

121 W. Zhu, S. Kattel, F. Jiao and J. G. Chen, *Adv. Energy Mater.*, 2019, **9**, 1802840.

122 H. Dong, L. Zhang, P. Yang, X. Chang, W. Zhu, X. Ren, Z.-J. Zhao and J. Gong, *Chem. Eng. Sci.*, 2019, **194**, 29–35.

123 Z. Han, C. Choi, H. Tao, Q. Fan, Y. Gao, S. Liu, A. W. Robertson, S. Hong, Y. Jung and Z. Sun, *Catal. Sci. Technol.*, 2018, **8**, 3894–3900.

124 R. Hegner, L. F. M. Rosa and F. Harnisch, *Appl. Catal., B*, 2018, **238**, 546–556.

125 Z. Xia, M. Freeman, D. Zhang, B. Yang, L. Lei, Z. Li and Y. Hou, *ChemElectroChem*, 2018, **5**, 253–259.

126 W. Yang, Y. Zhao, S. Chen, W. Ren, X. Chen, C. Jia, Z. Su, Y. Wang and C. Zhao, *Inorg. Chem.*, 2020, **59**, 12437–12444.

127 K. Mou, Z. Chen, S. Yao and L. Liu, *Electrochim. Acta*, 2018, **289**, 65–71.

128 P. Lu, X. Tan, H. Zhao, Q. Xiang, K. Liu, X. Zhao, X. Yin, X. Li, X. Hai, S. Xi, A. T. S. Wee, S. J. Pennycook, X. Yu, M. Yuan, J. Wu, G. Zhang, S. C. Smith and Z. Yin, *ACS Nano*, 2021, **15**, 5671–5678.

129 D. H. Won, C. H. Choi, J. Chung, M. W. Chung, E.-H. Kim and S. I. Woo, *ChemSusChem*, 2015, **8**, 3092–3098.

130 S. Zhang, P. Kang and T. J. Meyer, *J. Am. Chem. Soc.*, 2014, **136**, 1734–1737.

131 Y. Wang, C. Niu and D. Wang, *J. Colloid Interface Sci.*, 2018, **527**, 95–106.

132 X. An, S. Li, A. Yoshida, Z. Wang, X. Hao, A. Abudula and G. Guan, *ACS Sustainable Chem. Eng.*, 2019, **7**, 9360–9368.

133 Y. Zhang, L. Chen, F. Li, C. D. Easton, J. Li, A. M. Bond and J. Zhang, *ACS Catal.*, 2017, **7**, 4846–4853.

134 A. Katoh, H. Uchida, M. Shibata and M. Watanabe, *J. Electrochem. Soc.*, 1994, **141**, 2054–2058.

135 J. He, K. E. Dettelbach, A. Huang and C. P. Berlinguette, *Angew. Chem., Int. Ed.*, 2017, **56**, 16579–16582.

136 D. Li, L. Huang, Y. Tian, T. Liu, L. Zhen and Y. Feng, *Appl. Catal., B*, 2021, **292**, 120119.

137 Y. Xiong, B. Wei, M. Wu, B. Hu, F. Zhu, J. Hao and W. Shi, *J. CO2 Util.*, 2021, **51**, 101621.

138 Z. Tao, Z. Wu, X. Yuan, Y. Wu and H. Wang, *ACS Catal.*, 2019, **9**, 10894–10898.

139 X. Jiang, X. Wang, Z. Liu, Q. Wang, X. Xiao, H. Pan, M. Li, J. Wang, Y. Shao, Z. Peng, Y. Shen and M. Wang, *Appl. Catal., B*, 2019, **259**, 118040.

140 C. Chen, Y. Pang, F. Zhang, J. Zhong, B. Zhang and Z. Cheng, *J. Mater. Chem. A*, 2018, **6**, 19621–19630.

141 M. Zhang, Z. Zhang, Z. Zhao, H. Huang, D. H. Anjum, D. Wang, J.-h. He and K.-W. Huang, *ACS Catal.*, 2021, **11**, 11103–11108.

142 Q. Xie, G. O. Larrazábal, M. Ma, I. Chorkendorff, B. Seger and J. Luo, *J. Energy Chem.*, 2021, **63**, 278–284.

143 Z. Yang, H. Wang, X. Fei, W. Wang, Y. Zhao, X. Wang, X. Tan, Q. Zhao, H. Wang, J. Zhu, L. Zhou, H. Ning and M. Wu, *Appl. Catal., B*, 2021, **298**, 120571.

144 A. W. Kahsay, K. B. Ibrahim, M.-C. Tsai, M. K. Birhanu, S. A. Chala, W.-N. Su and B.-J. Hwang, *Catal. Lett.*, 2019, **149**, 860–869.

145 Z. Zhang, W. Liu, W. Zhang, M. Liu and S. Huo, *Colloids Surf., A*, 2021, **631**, 127637.

146 T. Shinagawa, G. O. Larrazábal, A. J. Martín, F. Krumeich and J. Pérez-Ramírez, *ACS Catal.*, 2018, **8**, 837–844.

147 J. Du, Y. Xin, M. Dong, J. Yang, Q. Xu, H. Liu and B. Han, *Small*, 2021, **17**, 2102629.

148 Y. Huang, Y. Deng, A. D. Handoko, G. K. L. Goh and B. S. Yeo, *ChemSusChem*, 2018, **11**, 320–326.

149 Y. Wang, Y. Chen, Y. Zhao, J. Yu, Z. Liu, Y. Shi, H. Liu, X. Li and W. Zhou, *Appl. Catal., B*, 2022, **307**, 120991.

150 J. Lim, A. T. Garcia-Esparza, J. W. Lee, G. Kang, S. Shin, S. S. Jeon and H. Lee, *Nanoscale*, 2022, **14**, 9297–9303.

151 W. Lou, L. Peng, R. He, Y. Liu and J. Qiao, *J. Colloid Interface Sci.*, 2022, **606**, 994–1003.

152 H. Hu, Y. Tang, Q. Hu, P. Wan, L. Dai and X. J. Yang, *Appl. Surf. Sci.*, 2018, **445**, 281–286.

153 P. Moreno-García, N. Schlegel, A. Zanetti, A. C. López, M. d. J. Gálvez-Vázquez, A. Dutta, M. Rahaman and P. Broekmann, *ACS Appl. Mater. Interfaces*, 2018, **10**, 31355–31365.

154 S. Lamaison, D. Wakerley, D. Montero, G. Rousse, D. Taverna, D. Giaume, D. Mercier, J. Blanchard, H. N. Tran, M. Fontecave and V. Mougel, *ChemSusChem*, 2019, **12**, 511–517.

155 J. Christophe, T. Doneux and C. Buess-Herman, *Electrocatalysis*, 2012, **3**, 139–146.

156 D. Kim, J. Resasco, Y. Yu, A. M. Asiri and P. Yang, *Nat. Commun.*, 2014, **5**, 4948.

157 D. Kim, C. Xie, N. Becknell, Y. Yu, M. Karamad, K. Chan, E. J. Crumlin, J. K. Nørskov and P. Yang, *J. Am. Chem. Soc.*, 2017, **139**, 8329–8336.

158 Z. Yin, D. Gao, S. Yao, B. Zhao, F. Cai, L. Lin, P. Tang, P. Zhai, G. Wang, D. Ma and X. Bao, *Nano Energy*, 2016, **27**, 35–43.

159 M. Li, J. Wang, P. Li, K. Chang, C. Li, T. Wang, B. Jiang, H. Zhang, H. Liu, Y. Yamauchi, N. Umezawa and J. Ye, *J. Mater. Chem. A*, 2016, **4**, 4776–4782.

160 Y. Mun, S. Lee, A. Cho, S. Kim, J. W. Han and J. Lee, *Appl. Catal., B*, 2019, **246**, 82–88.

161 V. S. S. Mosali, L. Li, G. Puxty, M. D. Horne, A. M. Bond and J. Zhang, *ChemElectroChem*, 2022, **9**, e202101227.

162 P. Bumroongsakulsawat and G. H. Kelsall, *Electrochim. Acta*, 2014, **141**, 216–225.

163 N. Han, Y. Wang, J. Deng, J. Zhou, Y. Wu, H. Yang, P. Ding and Y. Li, *J. Mater. Chem. A*, 2019, **7**, 1267–1272.

164 X. Lu, D. Y. C. Leung, H. Wang, M. K. H. Leung and J. Xuan, *ChemElectroChem*, 2014, **1**, 836–849.

165 T. Yuan, Z. Hu, Y. Zhao, J. Fang, J. Lv, Q. Zhang, Z. Zhuang, L. Gu and S. Hu, *Nano Lett.*, 2020, **20**, 2916–2922.

166 W. Ma, S. Xie, X.-G. Zhang, F. Sun, J. Kang, Z. Jiang, Q. Zhang, D.-Y. Wu and Y. Wang, *Nat. Commun.*, 2019, **10**, 892.

167 J. He, X. Liu, H. Liu, Z. Zhao, Y. Ding and J. Luo, *J. Catal.*, 2018, **364**, 125–130.

168 X. Zheng, P. De Luna, F. P. García de Arquer, B. Zhang, N. Becknell, M. B. Ross, Y. Li, M. N. Banis, Y. Li, M. Liu, O. Voznyy, C. T. Dinh, T. Zhuang, P. Stadler, Y. Cui, X. Du, P. Yang and E. H. Sargent, *Joule*, 2017, **1**, 794–805.

169 Q. Li, J. Fu, W. Zhu, Z. Chen, B. Shen, L. Wu, Z. Xi, T. Wang, G. Lu, J.-j. Zhu and S. Sun, *J. Am. Chem. Soc.*, 2017, **139**, 4290–4293.

170 H. Xie, S. Chen, F. Ma, J. Liang, Z. Miao, T. Wang, H.-L. Wang, Y. Huang and Q. Li, *ACS Appl. Mater. Interfaces*, 2018, **10**, 36996–37004.

171 G. O. Larrazábal, T. Shinagawa, A. J. Martín and J. Pérez-Ramírez, *Nat. Commun.*, 2018, **9**, 1477.

172 Y. Zhao, C. Wang and G. G. Wallace, *J. Mater. Chem. A*, 2016, **4**, 10710–10718.

173 S. Sarfraz, A. T. Garcia-Esparza, A. Jedidi, L. Cavallo and K. Takanabe, *ACS Catal.*, 2016, **6**, 2842–2851.

174 J. Zeng, K. Bejtka, W. Ju, M. Castellino, A. Chiodoni, A. Sacco, M. A. Farkhondehfal, S. Hernández, D. Rentsch, C. Battaglia and C. F. Pirri, *Appl. Catal., B*, 2018, **236**, 475–482.

175 S. Rasul, D. H. Anjum, A. Jedidi, Y. Minenkov, L. Cavallo and K. Takanabe, *Angew. Chem., Int. Ed.*, 2015, **54**, 2146–2150.

176 A. Jedidi, S. Rasul, D. Masih, L. Cavallo and K. Takanabe, *J. Mater. Chem. A*, 2015, **3**, 19085–19092.

177 G. O. Larrazábal, A. J. Martín, S. Mitchell, R. Hauert and J. Pérez-Ramírez, *ACS Catal.*, 2016, **6**, 6265–6274.

178 Y. Zhang, Z. Cai, Y. Zhao, X. Wen, W. Xu, Y. Zhong, L. Bai, W. Liu, Y. Zhang, Y. Zhang, Y. Kuang and X. Sun, *Nanoscale Horiz.*, 2019, **4**, 490–494.

179 X. Xiao, Y. Xu, X. Lv, J. Xie, J. Liu and C. Yu, *J. Colloid Interface Sci.*, 2019, **545**, 1–7.

180 W. Zheng, J. Yang, H. Chen, Y. Hou, Q. Wang, M. Gu, F. He, Y. Xia, Z. Xia, Z. Li, B. Yang, L. Lei, C. Yuan, Q. He, M. Qiu and X. Feng, *Adv. Funct. Mater.*, 2020, **30**, 1907658.

181 C. Jiménez, J. García, F. Martínez, R. Camarillo and J. Rincón, *Electrochim. Acta*, 2020, **337**, 135663.

182 B. Cho, J. Lee, I. P. Roh, M. H. Lee and T. Yu, *J. Alloys Compd.*, 2022, **911**, 164990.

183 J. Zeng, M. R. Fiorentin, M. Fontana, M. Castellino, F. Risplendi, A. Sacco, G. Cicero, M. A. Farkhondehfal, F. Drago and C. F. Pirri, *Appl. Catal., B*, 2022, **306**, 121089.

184 H. S. Jeon, J. Timoshenko, F. Scholten, I. Sinev, A. Herzog, F. T. Haase and B. R. Cuenya, *J. Am. Chem. Soc.*, 2019, **141**, 19879–19887.

185 Y. Wang, Z. Chen, P. Han, Y. Du, Z. Gu, X. Xu and G. Zheng, *ACS Catal.*, 2018, **8**, 7113–7119.

186 S. B. Varandili, J. Huang, E. Oveisi, G. L. De Gregorio, M. Mensi, M. Strach, J. Vavra, C. Gadiyar, A. Bhowmik and R. Buonsanti, *ACS Catal.*, 2019, **9**, 5035–5046.

187 C.-J. Chang, S.-C. Lin, H.-C. Chen, J. Wang, K. J. Zheng, Y. Zhu and H. M. Chen, *J. Am. Chem. Soc.*, 2020, **142**, 12119–12132.

188 Y. Qiu, H. Zhong, W. Xu, T. Zhang, X. Li and H. Zhang, *J. Mater. Chem. A*, 2019, **7**, 5453–5462.

189 G. Shi, Y. Xie, L. Du, X. Fu, X. Chen, W. Xie, T.-B. Lu, M. Yuan and M. Wang, *Angew. Chem., Int. Ed.*, 2022, **61**, e202203569.

190 H. Yang, Y. Wu, G. Li, Q. Lin, Q. Hu, Q. Zhang, J. Liu and C. He, *J. Am. Chem. Soc.*, 2019, **141**, 12717–12723.

191 G. L. De Gregorio, T. Burdyny, A. Loiudice, P. Iyengar, W. A. Smith and R. Buonsanti, *ACS Catal.*, 2020, **10**, 4854–4862.

192 D. Bagchi, J. Raj, A. K. Singh, A. Cherevotan, S. Roy, K. S. Manoj, C. P. Vinod and S. C. Peter, *Adv. Mater.*, 2022, **34**, 2109426.

193 M. Watanabe, M. Shibata, A. Katoh, T. Sakata and M. Azuma, *J. Electroanal. Chem. Interfacial Electrochem.*, 1991, **305**, 319–328.

194 F. Jia, X. Yu and L. Zhang, *J. Power Sources*, 2014, **252**, 85–89.

195 J. Albo, A. Sáez, J. Solla-Gullón, V. Montiel and A. Irabien, *Appl. Catal., B*, 2015, **176–177**, 709–717.

196 T.-C. Chou, C.-C. Chang, H.-L. Yu, W.-Y. Yu, C.-L. Dong, J.-J. Velasco-Vélez, C.-H. Chuang, L.-C. Chen, J.-F. Lee, J.-M. Chen and H.-L. Wu, *J. Am. Chem. Soc.*, 2020, **142**, 2857–2867.

197 J. Wang, H.-Y. Tan, Y. Zhu, H. Chu and H. M. Chen, *Angew. Chem., Int. Ed.*, 2021, **60**, 17254–17267.

198 P.-P. Yang, X.-L. Zhang, F.-Y. Gao, Y.-R. Zheng, Z.-Z. Niu, X. Yu, R. Liu, Z.-Z. Wu, S. Qin, L.-P. Chi, Y. Duan, T. Ma, X.-S. Zheng, J.-F. Zhu, H.-J. Wang, M.-R. Gao and S.-H. Yu, *J. Am. Chem. Soc.*, 2020, **142**, 6400–6408.

199 Q. Lei, H. Zhu, K. Song, N. Wei, L. Liu, D. Zhang, J. Yin, X. Dong, K. Yao, N. Wang, X. Li, B. Davaasuren, J. Wang and Y. Han, *J. Am. Chem. Soc.*, 2020, **142**, 4213–4222.

200 S. H. Lee, J. C. Lin, M. Farmand, A. T. Landers, J. T. Feaster, E. A. Acosta, J. W. Beeman, Y. Ye, J. Yano, A. Mehta, R. C. Davis, T. F. Jaramillo, C. Hahn and W. S. Drisdell, *J. Am. Chem. Soc.*, 2021, **143**, 588–592.

201 Y. Feng, Z. Li, H. Liu, C. Dong, J. Wang, S. A. Kulinich and X. Du, *Langmuir*, 2018, **34**, 13544–13549.

202 I. Merino-Garcia, J. Albo, J. Solla-Gullón, V. Montiel and A. Irabien, *J. CO2 Util.*, 2019, **31**, 135–142.

203 T. Zhang, Z. Li, J. Zhang and J. Wu, *J. Catal.*, 2020, **387**, 163–169.

204 T. T. H. Hoang, S. Verma, S. Ma, T. T. Fister, J. Timoshenko, A. I. Frenkel, P. J. A. Kenis and A. A. Gewirth, *J. Am. Chem. Soc.*, 2018, **140**, 5791–5797.

205 C. S. Chen, J. H. Wan and B. S. Yeo, *J. Phys. Chem. C*, 2015, **119**, 26875–26882.

206 P.-P. Guo, Z.-H. He, S.-Y. Yang, W. Wang, K. Wang, C.-C. Li, Y.-Y. Wei, Z.-T. Liu and B. Han, *Green Chem.*, 2022, **24**, 1527–1533.

207 Y. Chen, Z. Fan, J. Wang, C. Ling, W. Niu, Z. Huang, G. Liu, B. Chen, Z. Lai, X. Liu, B. Li, Y. Zong, L. Gu, J. Wang, X. Wang and H. Zhang, *J. Am. Chem. Soc.*, 2020, **142**, 12760–12766.

208 T. Akter, H. Pan and C. J. Barile, *J. Phys. Chem. C*, 2022, **126**, 10045–10052.

209 J. Huang, M. Mensi, E. Oveisi, V. Mantella and R. Buonsanti, *J. Am. Chem. Soc.*, 2019, **141**, 2490–2499.

210 S. Y. Lee, H. Jung, N.-K. Kim, H.-S. Oh, B. K. Min and Y. J. Hwang, *J. Am. Chem. Soc.*, 2018, **140**, 8681–8689.

211 H. Mistry, A. S. Varela, C. S. Bonifacio, I. Zegkinoglou, I. Sinev, Y.-W. Choi, K. Kisslinger, E. A. Stach, J. C. Yang, P. Strasser and B. R. Cuenya, *Nat. Commun.*, 2016, **7**, 12123.

212 A. D. Handoko, C. W. Ong, Y. Huang, Z. G. Lee, L. Lin, G. B. Panetti and B. S. Yeo, *J. Phys. Chem. C*, 2016, **120**, 20058–20067.

213 B. Zhang, J. Zhang, M. Hua, Q. Wan, Z. Su, X. Tan, L. Liu, F. Zhang, G. Chen, D. Tan, X. Cheng, B. Han, L. Zheng and G. Mo, *J. Am. Chem. Soc.*, 2020, **142**, 13606–13613.

214 D. Ren, Y. Deng, A. D. Handoko, C. S. Chen, S. Malkhandi and B. S. Yeo, *ACS Catal.*, 2015, **5**, 2814–2821.

215 C. S. Chen, A. D. Handoko, J. H. Wan, L. Ma, D. Ren and B. S. Yeo, *Catal. Sci. Technol.*, 2015, **5**, 161–168.

216 Y. Zhou, F. Che, M. Liu, C. Zou, Z. Liang, P. De Luna, H. Yuan, J. Li, Z. Wang, H. Xie, H. Li, P. Chen, E. Bladt, R. Quintero-Bermudez, T.-K. Sham, S. Bals, J. Hofkens, D. Sinton, G. Chen and E. H. Sargent, *Nat. Chem.*, 2018, **10**, 974–980.

217 D. Gao, I. Zegkinoglou, N. J. Divins, F. Scholten, I. Sinev, P. Grosse and B. R. Cuenya, *ACS Nano*, 2017, **11**, 4825–4831.

218 Y. Gao, Q. Wu, X. Liang, Z. Wang, Z. Zheng, P. Wang, Y. Liu, Y. Dai, M.-H. Whangbo and B. Huang, *Adv. Sci.*, 2020, **7**, 1902820.

219 H. Jung, S. Y. Lee, C. W. Lee, M. K. Cho, D. H. Won, C. Kim, H.-S. Oh, B. K. Min and Y. J. Hwang, *J. Am. Chem. Soc.*, 2019, **141**, 4624–4633.

220 Z. Yin, C. Yu, Z. Zhao, X. Guo, M. Shen, N. Li, M. Muzzio, J. Li, H. Liu, H. Lin, J. Yin, G. Lu, D. Su and S. Sun, *Nano Lett.*, 2019, **19**, 8658–8663.

221 J. Zhang, Z. Liu, H. Guo, H. Lin, H. Wang, X. Liang, H. Hu, Q. Xia, X. Zou and X. Huang, *ACS Appl. Mater. Interfaces*, 2022, **14**, 19388–19396.

222 F. Yang, W. Fang, Q. Wang, P. Deng and B. Y. Xia, *ACS Sustainable Chem. Eng.*, 2022, **10**, 4677–4682.

223 X. Li, J. Wang, X. Lv, Y. Yang, Y. Xu, Q. Liu and H. B. Wu, *Nano-Micro Lett.*, 2022, **14**, 134.

224 H. Wang, E. Matios, C. Wang, J. Luo, X. Lu, X. Hu and W. Li, *Nano Lett.*, 2019, **19**, 3925–3932.

225 Z.-Q. Liang, T.-T. Zhuang, A. Seifitokaldani, J. Li, C.-W. Huang, C.-S. Tan, Y. Li, P. De Luna, C. T. Dinh, Y. Hu, Q. Xiao, P.-L. Hsieh, Y. Wang, F. Li, R. Quintero-Bermudez, Y. Zhou, P. Chen, Y. Pang, S.-C. Lo, L.-J. Chen, H. Tan, Z. Xu, S. Zhao, D. Sinton and E. H. Sargent, *Nat. Commun.*, 2018, **9**, 3828.

226 J. Han, C. Long, J. Zhang, K. Hou, Y. Yuan, D. Wang, X. Zhang, X. Qiu, Y. Zhu, Y. Zhang, Z. Yang, S. Yan and Z. Tang, *Chem. Sci.*, 2020, **11**, 10698–10704.

227 Y. Mi, X. Peng, X. Liu and J. Luo, *ACS Appl. Energy Mater.*, 2018, **1**, 5119–5123.

228 C. Choi, S. Kwon, T. Cheng, M. Xu, P. Tieu, C. Lee, J. Cai, H. M. Lee, X. Pan, X. Duan, W. A. Goddard and Y. Huang, *Nat. Catal.*, 2020, **3**, 804–812.

229 A. Stalinraja, K. Gopalram, S. Venkatesan, S. M. J. S. Ghosh and T. Selvaraj, *Electrochim. Acta*, 2022, **431**, 141078.

230 J. Shan, Y. Shi, H. Li, Z. Chen, C. Sun, Y. Shuai and Z. Wang, *Chem. Eng. J.*, 2022, **433**, 133769.

231 Y. C. Li, Z. Wang, T. Yuan, D.-H. Nam, M. Luo, J. Wicks, B. Chen, J. Li, F. Li, F. P. G. de Arquer, Y. Wang, C.-T. Dinh, O. Voznyy, D. Sinton and E. H. Sargent, *J. Am. Chem. Soc.*, 2019, **141**, 8584–8591.

232 T. T. H. Hoang, S. Ma, J. I. Gold, P. J. A. Kenis and A. A. Gewirth, *ACS Catal.*, 2017, **7**, 3313–3321.

233 S. Ma, M. Sadakiyo, R. Luo, M. Heima, M. Yamauchi and P. J. A. Kenis, *J. Power Sources*, 2016, **301**, 219–228.

234 C.-T. Dinh, T. Burdyny, M. G. Kibria, A. Seifitokaldani, C. M. Gabardo, F. P. García de Arquer, A. Kiani, J. P. Edwards, P. De Luna, O. S. Bushuyev, C. Zou, R. Quintero-Bermudez, Y. Pang, D. Sinton and E. H. Sargent, *Science*, 2018, **360**, 783–787.

235 W. Liu, P. Zhai, A. Li, B. Wei, K. Si, Y. Wei, X. Wang, G. Zhu, Q. Chen, X. Gu, R. Zhang, W. Zhou and Y. Gong, *Nat. Commun.*, 2022, **13**, 1877.

236 W. Ma, S. Xie, T. Liu, Q. Fan, J. Ye, F. Sun, Z. Jiang, Q. Zhang, J. Cheng and Y. Wang, *Nat. Catal.*, 2020, **3**, 478–487.

237 T.-T. Zhuang, Z.-Q. Liang, A. Seifitokaldani, Y. Li, P. De Luna, T. Burdyny, F. Che, F. Meng, Y. Min, R. Quintero-Bermudez, C. T. Dinh, Y. Pang, M. Zhong, B. Zhang, J. Li, P.-N. Chen, X.-L. Zheng, H. Liang, W.-N. Ge, B.-J. Ye, D. Sinton, S.-H. Yu and E. H. Sargent, *Nat. Catal.*, 2018, **1**, 421–428.

238 P. De Luna, R. Quintero-Bermudez, C.-T. Dinh, M. B. Ross, O. S. Bushuyev, P. Todorović, T. Regier, S. O. Kelley, P. Yang and E. H. Sargent, *Nat. Catal.*, 2018, **1**, 103–110.

239 J.-J. Lv, M. Jouny, W. Luc, W. Zhu, J.-J. Zhu and F. Jiao, *Adv. Mater.*, 2018, **30**, 1803111.

240 Y. Xu, J. P. Edwards, S. Liu, R. K. Miao, J. E. Huang, C. M. Gabardo, C. P. O'Brien, J. Li, E. H. Sargent and D. Sinton, *ACS Energy Lett.*, 2021, **6**, 809–815.

241 F. Li, A. Thevenon, A. Rosas-Hernández, Z. Wang, Y. Li, C. M. Gabardo, A. Ozden, C. T. Dinh, J. Li, Y. Wang, J. P. Edwards, Y. Xu, C. McCallum, L. Tao, Z.-Q. Liang, M. Luo, X. Wang, H. Li, C. P. O'Brien, C.-S. Tan, D.-H. Nam, R. Quintero-Bermudez, T.-T. Zhuang, Y. C. Li, Z. Han, R. D. Britt, D. Sinton, T. Agapie, J. C. Peters and E. H. Sargent, *Nature*, 2020, **577**, 509–513.

242 C. M. Gabardo, C. P. O'Brien, J. P. Edwards, C. McCallum, Y. Xu, C.-T. Dinh, J. Li, E. H. Sargent and D. Sinton, *Joule*, 2019, **3**, 2777–2791.

243 D. Ren, B. S.-H. Ang and B. S. Yeo, *ACS Catal.*, 2016, **6**, 8239–8247.

244 D. Ren, J. Gao, L. Pan, Z. Wang, J. Luo, S. M. Zakeeruddin, A. Hagfeldt and M. Grätzel, *Angew. Chem., Int. Ed.*, 2019, **58**, 15036–15040.

245 C.-J. Chang, S.-F. Hung, C.-S. Hsu, H.-C. Chen, S.-C. Lin, Y.-F. Liao and H. M. Chen, *ACS Cent. Sci.*, 2019, **5**, 1998–2009.

246 L. Shang, X. Lv, L. Zhong, S. Li and G. Zheng, *Small Methods*, 2022, **6**, 2101334.

247 L. R. L. Ting, O. Piqué, S. Y. Lim, M. Tanhaei, F. Calle-Vallejo and B. S. Yeo, *ACS Catal.*, 2020, **10**, 4059–4069.

248 S. Shen, X. Peng, L. Song, Y. Qiu, C. Li, L. Zhuo, J. He, J. Ren, X. Liu and J. Luo, *Small*, 2019, **15**, 1902229.

249 X. Su, Y. Sun, L. Jin, L. Zhang, Y. Yang, P. Kerns, B. Liu, S. Li and J. He, *Appl. Catal., B*, 2020, **269**, 118800.

250 Q. Zhu, X. Sun, D. Yang, J. Ma, X. Kang, L. Zheng, J. Zhang, Z. Wu and B. Han, *Nat. Commun.*, 2019, **10**, 3851.

251 D. Chi, H. Yang, Y. Du, T. Lv, G. Sui, H. Wang and J. Lu, *RSC Adv.*, 2014, **4**, 37329–37332.

252 Y. Song, R. Peng, D. K. Hensley, P. V. Bonnesen, L. Liang, Z. Wu, H. M. Meyer III, M. Chi, C. Ma, B. G. Sumpter and A. J. Rondinone, *ChemistrySelect*, 2016, **1**, 6055–6061.

253 D. Gao, I. Sinev, F. Scholten, R. M. Arán-Ais, N. J. Divins, K. Kvashnina, J. Timoshenko and B. R. Cuenya, *Angew. Chem., Int. Ed.*, 2019, **58**, 17047–17053.

254 Y. Zhang, K. Li, M. Chen, J. Wang, J. Liu and Y. Zhang, *ACS Appl. Nano Mater.*, 2020, **3**, 257–263.

255 X. Su, Z. Jiang, J. Zhou, H. Liu, D. Zhou, H. Shang, X. Ni, Z. Peng, F. Yang, W. Chen, Z. Qi, D. Wang and Y. Wang, *Nat. Commun.*, 2022, **13**, 1322.

256 Y. Baek, H. Song, D. Hong, S. Wang, S. Lee, Y.-C. Joo, G.-D. Lee and J. Oh, *J. Mater. Chem. A*, 2022, **10**, 9393–9401.

257 W. Su, L. Ma, Q. Cheng, K. Wen, P. Wang, W. Hu, L. Zou, J. Fang and H. Yang, *J. CO2 Util.*, 2021, **52**, 101698.

258 X. Zhang, C. Liu, Y. Zhao, L. Li, Y. Chen, F. Raziq, L. Qiao, S.-X. Guo, C. Wang, G. G. Wallace, A. M. Bond and J. Zhang, *Appl. Catal., B*, 2021, **291**, 120030.

259 X. Wang, Z. Wang, F. P. García de Arquer, C.-T. Dinh, A. Ozden, Y. C. Li, D.-H. Nam, J. Li, Y.-S. Liu, J. Wicks, Z. Chen, M. Chi, B. Chen, Y. Wang, J. Tam, J. Y. Howe, A. Proppe, P. Todorović, F. Li, T.-T. Zhuang, C. M. Gabardo, A. R. Kirmani, C. McCallum, S.-F. Hung, Y. Lum, M. Luo, Y. Min, A. Xu, C. P. O'Brien, B. Stephen, B. Sun, A. H. Ip, L. J. Richter, S. O. Kelley, D. Sinton and E. H. Sargent, *Nat. Energy*, 2020, **5**, 478–486.

260 Z. Gu, H. Shen, Z. Chen, Y. Yang, C. Yang, Y. Ji, Y. Wang, C. Zhu, J. Liu, J. Li, T.-K. Sham, X. Xu and G. Zheng, *Joule*, 2021, **5**, 429–440.

261 F. Li, Y. C. Li, Z. Wang, J. Li, D.-H. Nam, Y. Lum, M. Luo, X. Wang, A. Ozden, S.-F. Hung, B. Chen, Y. Wang, J. Wicks, Y. Xu, Y. Li, C. M. Gabardo, C.-T. Dinh, Y. Wang, T.-T. Zhuang, D. Sinton and E. H. Sargent, *Nat. Catal.*, 2020, **3**, 75–82.

262 Y. Lum and J. W. Ager, *Energy Environ. Sci.*, 2018, **11**, 2935–2944.

263 C. G. Morales-Guio, E. R. Cave, S. A. Nitopi, J. T. Feaster, L. Wang, K. P. Kuhl, A. Jackson, N. C. Johnson, D. N. Abram, T. Hatsukade, C. Hahn and T. F. Jaramillo, *Nat. Catal.*, 2018, **1**, 764–771.

264 D. Zang, Q. Li, G. Dai, M. Zeng, Y. Huang and Y. Wei, *Appl. Catal., B*, 2021, **281**, 119426.

265 P. Wang, H. Yang, Y. Xu, X. Huang, J. Wang, M. Zhong, T. Cheng and Q. Shao, *ACS Nano*, 2021, **15**, 1039–1047.

266 C. Azenha, C. Mateos-Pedrero, M. Alvarez-Guerra, A. Irabien and A. Mendes, *Chem. Eng. J.*, 2022, **445**, 136575.

267 Y. Wang, D. Wang, C. J. Dares, S. L. Marquard, M. V. Sheridan and T. J. Meyer, *Proc. Natl. Acad. Sci. U. S. A.*, 2018, **115**, 278–283.

268 K. Zhao, X. Nie, H. Wang, S. Chen, X. Quan, H. Yu, W. Choi, G. Zhang, B. Kim and J. G. Chen, *Nat. Commun.*, 2020, **11**, 2455.

269 C. Peng, G. Luo, J. Zhang, M. Chen, Z. Wang, T.-K. Sham, L. Zhang, Y. Li and G. Zheng, *Nat. Commun.*, 2021, **12**, 1580.

270 R. A. Geioushy, M. M. Khaled, K. Alhooshani, A. S. Hakeem and A. Rinaldi, *Electrochim. Acta*, 2017, **245**, 456–462.

271 A. V. Rayer, E. Reid, A. Kataria, I. Luz, S. J. Thompson, M. Lail, J. Zhou and M. Soukri, *J. CO2 Util.*, 2020, **39**, 101159.

272 T. Toyao, Z. Maeno, S. Takakusagi, T. Kamachi, I. Takigawa and K.-i. Shimizu, *ACS Catal.*, 2020, **10**, 2260–2297.

273 J. R. Kitchin, *Nat. Catal.*, 2018, **1**, 230–232.

274 Y. Sun and S. Dai, *Sci. Adv.*, 2021, **7**, eabg1600.

275 H. Liu, L. Syama, L. Zhang, C. Lee, C. Liu, Z. Dai and Q. Yan, *SusMat*, 2021, **1**, 482–505.

276 D. Roy, S. C. Mandal and B. Pathak, *J. Phys. Chem. Lett.*, 2022, **13**, 5991–6002.

277 S. Nellaiappan, N. K. Katiyar, R. Kumar, A. Parui, K. D. Malviya, K. G. Pradeep, A. K. Singh, S. Sharma, C. S. Tiwary and K. Biswas, *ACS Catal.*, 2020, **10**, 3658–3663.

278 S.-X. Guo, C. L. Bentley, M. Kang, A. M. Bond, P. R. Unwin and J. Zhang, *Acc. Chem. Res.*, 2022, 23–34.

279 Y. Zhang, S.-X. Guo, X. Zhang, A. M. Bond and J. Zhang, *Nano Today*, 2020, **31**, 100835.

280 Z. W. Seh, J. Kibsgaard, C. F. Dickens, I. Chorkendorff, J. K. Nørskov and T. F. Jaramillo, *Science*, 2017, **355**, eaad4998.

281 R. Yang, J. Duan, P. Dong, Q. Wen, M. Wu, Y. Liu, Y. Liu, H. Li and T. Zhai, *Angew. Chem., Int. Ed.*, 2022, **61**, e202116706.

282 D. Higgins, C. Hahn, C. Xiang, T. F. Jaramillo and A. Z. Weber, *ACS Energy Lett.*, 2019, **4**, 317–324.

283 L. Ge, H. Rabiee, M. Li, S. Subramanian, Y. Zheng, J. H. Lee, T. Burdyny and H. Wang, *Chem*, 2022, **8**, 663–692.

284 S. Overa, B. H. Ko, Y. Zhao and F. Jiao, *Acc. Chem. Res.*, 2022, **55**, 638–648.